

Collective bursting of free surface bubbles, and the role of surface contamination

B. Néel^{1,†} and L. Deike^{1,2,‡}

¹Department of Mechanical and Aerospace Engineering, Princeton University, Princeton, NJ 08544, USA

²High Meadows Environmental Institute, Princeton University, Princeton, NJ 08544, USA

(Received xx; revised xx; accepted xx)

Air bubbles at the surface of water end their life in a particular way: when bursting, they may eject drops of liquid in the surrounding environment. Many uncertainties remain regarding collective effects of bubbles at the water-air interface, despite extensive efforts to describe the bursting mechanisms, motivated by their critical importance in mass transfers between the ocean and the atmosphere in the production of sea spray aerosols. We investigate the effect of surfactant on the collective dynamics and statistics of air bubbles evolving freely at the surface of water, through an experimental setup controlling the bulk distribution of bubbles with nearly monodisperse millimetric air bubbles. We observe that for low contamination, bubble coalescence is inevitable and lead to a broad surface size distribution. For higher surfactant concentrations, coalescence at the surface is prevented and bubble lifetime is increased, leading to the formation of rafts with a surface size distribution identical to the bulk distribution. This shows that surface contamination has a first-order influence on the transfer function from *bulk* size distribution to *surface* size distribution, an intermediate step which needs to be considered when developing sea spray source function as droplet production by bubble bursting depends on the bubble size. We measure the bursting and merging rates of bubbles as a function of contamination through a complementary freely decaying raft experiment. We propose a cellular automaton model that includes the minimal ingredients to reproduce the experimental results in the statistically stationary configuration: production, coalescence and bursting after a finite lifetime.

1. Introduction

1.1. The broader context

Gas bubbles bursting at the surface of a liquid are known, under the appropriate conditions, to eject drops in their surrounding environment. It is not only a fascinating problem *per se*, but also important to understand for its ubiquitous applications: diseases and pathogens transport (Poulain & Bourouiba 2019), lava bubble bursting (Wilson 1980; Vergnolle & Brandeis 1996; Gonnermann & Manga 2007), formation of condensation nuclei (Woodcock *et al.* 1953), champagne aroma transport (Ghabache *et al.* 2016), and their broader role in liquid fragmentation (Villermaux 2007).

In the open sea, such drops are propelled in the atmospheric boundary layer, where they may travel upwards for times much longer than their gravity settling time in a quiescent atmosphere. Constituted of sea water, these spray drops carry salts (among other materials), which remain in suspension in the atmosphere once the liquid has

† Email address for correspondence: neel.b@princeton.edu

‡ Email address for correspondence: ldeike@princeton.edu

evaporated. This way, bubbles bursting at the surface of the ocean contribute to sea spray aerosols, whose implication as cloud condensation nuclei, has long been established, since the pioneering works of Coulier (1875); Aitken (1880), and later Blanchard (1954); Mason (1971). Their precise chemical composition and role in atmospheric processes remains an active area of research (DeMott *et al.* 2016; Cochran *et al.* 2017), and requires an understanding of the production processes.

1.2. Sea spray aerosols: the quest for parameterization

One of the related challenges in ocean and atmospheric sciences has long been to parameterize accurately the sea spray aerosols production, through the use of a sea spray generation function. Classic sea spray generation functions depend on meteorological parameters, primarily the wind speed (Fairall *et al.* 1994; Lewis & Schwartz 2004), but significant scatter remains in current formulations, in parts due to the large range of scales involved (de Leeuw *et al.* 2011; Veron 2015). Sea spray generation is related to surface breaking waves, either directly during wave impact and atomization by wind shear (Veron *et al.* 2012; Erinin *et al.* 2019), or through bubble bursting following air entrainment by breaking (Deike *et al.* 2016, 2017; Deike & Melville 2018) so that the sea state modulates the droplet production (Lenain & Melville 2017), together with the precise ocean water temperature and composition (salinity, biological activity, etc) which will impact interfacial phenomena (Wang *et al.* 2017; Frossard *et al.* 2019).

1.3. Bubbles at the surface

In this oceanographic context of sea spray production, bubble bursting mechanisms have been singled out and identified, as reviewed by Veron (2015) and illustrated in figure 1. *Jet drops* are produced when the bubble cavity collapses and forms a vertical upward jet that destabilizes into drops (Blanchard 1954; Duchemin *et al.* 2002; Ghabache *et al.* 2014; Gañán-Calvo 2017; Brasz *et al.* 2018; Deike *et al.* 2018; Lai *et al.* 2018; Berny *et al.* 2020; Blanco-Rodríguez & Gordillo 2020). The mechanism concerns mostly small bubbles, when compared to the capillary length $\ell_c = \sqrt{\gamma/\rho g}$ ($= 2.7$ mm in water), with ρ the water density, γ the air-water interfacial tension, and g the gravitational acceleration (Jurin 1717). It is thus dominated by capillarity, and occurs on the inertio-capillary timescale $\tau_c = \sqrt{\rho d^3/\gamma}$, with d the bubble diameter.

Film drops are generated by the puncture, retraction and destabilization of the thin cap of mainly big bubbles with $d > \ell_c$ (Blanchard & Syzdek 1988; Spiel 1998; Lhuissier & Villermaux 2012; Poulain *et al.* 2018). Capillarity once again dominates the dynamics, by setting the retraction velocity of the film: $V = \sqrt{2\gamma/\rho h}$ (Taylor 1959; Culick 1960) and thus the relevant timescale $\tau_{TC} = \sqrt{\rho h d^2/\gamma}$, with h the cap film thickness.

Figure 1 illustrates bubble plumes generated by breaking waves at the ocean surface, seen from above. The presence of whitecaps indicates that the bubbles, once they have reached the surface, do not burst immediately, but instead spend some time there, much longer than the scales τ_c and τ_{TC} . Figure 1b shows the different timescales involved on a single schematic scale, starting with the fast bursting and coalescence scales, driven by capillarity (10 ms and below, Vella & Mahadevan (2005); Paulsen *et al.* (2014)), up to the slower scales of bubbles rising in the plume (Clift *et al.* 1978), drifting at the surface (Deike *et al.* 2016) and lifetimes (Poulain *et al.* 2018), from 0.1 s and longer. Surface bubbles thus evolve on a wide range of timescales, and all of which have to be taken into consideration for a complete understanding, as well as accurate parameterizations, of the sea spray production.

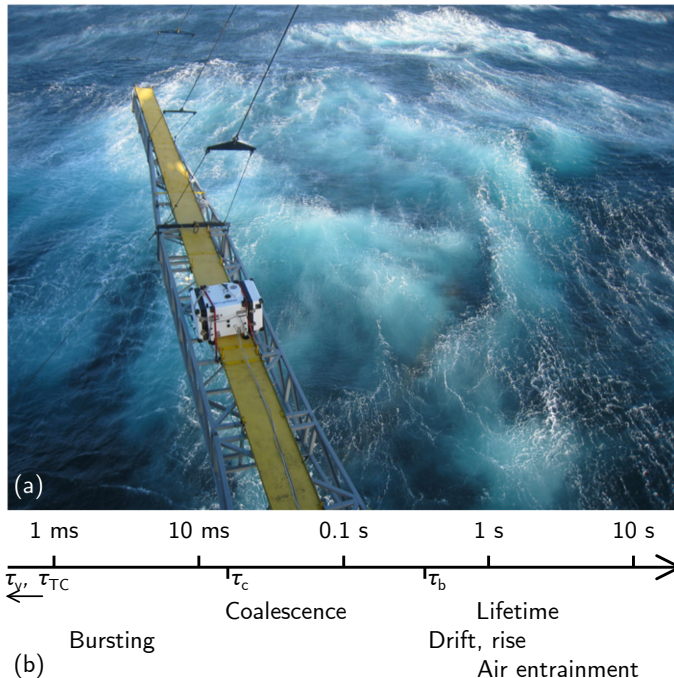


Figure 1: (a) Photograph taken after a large breaking event from R/P FLIP during the SoCal 2013 program off the coast of Southern California in November 2013. Bubbles activity at the ocean surface is clearly visible after the breaking event. (b) A schematic of the wide range of time scales involved in bubble processes at the surface is estimated for a typical bubble size $d = \ell_c$, the capillary size. The visco-capillary time $\tau_v = \mu d / \gamma \simeq 0.04$ ms and cap retraction time $\tau_{TC} = d / \sqrt{2\gamma / \rho h} \simeq 0.1$ ms are too short to appear in the diagram. $\tau_c = \sqrt{\rho d^3 / \gamma} \simeq 17$ ms is the inertio-capillary time, appearing in the reorganization of the bubble cavity at bursting and coalescence. $\langle \tau_s \rangle \propto \tau_v \sqrt{d / \ell_c} \simeq 0.7$ s is the typical surface bubble lifetime predicted by Poulain *et al.* (2018). Rising and drifting are estimated from a typical rise velocity of 0.1 ms^{-1} over distances of 0.1-1 m.

1.4. Surfactants and the physico-chemistry of the interface

The behavior of the ocean surface, partly covered by a biofilm, can be modeled with the help of surfactants, following the approach of Wurl *et al.* (2011) and benefiting from decades of research on the physico-chemistry of liquid-gas interfaces. Surface-active materials are known to modify the static and dynamic behaviors of a water-air interface in many different ways. Of primary interest to us, they favor foam stability by delaying or preventing bubbles coalescence (Garrett 1967; Oolman & Blanch 1986; Weaire & Hutzler 1999; Stevenson 2012; Cantat *et al.* 2013; Langevin & Rio 2015) and increasing bubbles lifetime (Modini *et al.* 2013; Poulain *et al.* 2018). They also readily dampen capillary waves (Franklin 1774; Liu & Duncan 2006), “rigidify” interfaces (Levich 1962), among important features still under active scrutiny.

In the oceanographic context, the composition of the sea-surface microlayer plays a major role in the later composition of the aerosols, hand to hand with the spray production mechanisms (Modini *et al.* 2013; Collins *et al.* 2014; Cochran *et al.* 2017; Wang *et al.* 2017). Multiple approaches have attempted to describe the role of the physico-chemical parameters on bubble bursting and the subsequent droplets and aerosols

production, with large variations in protocols and results sometimes contradicting each other. Frossard *et al.* (2019) describes a bubbles plume simulator, taken onboard of a cruise to produce an abundant sea spray with real time ocean conditions, and observes an increase in spray production with increased biological activity and inferred surfactant conditions. The laboratory experiment by Modini *et al.* (2013), which investigates the effect of surfactant on salt-water single bubble bursting, yields the opposite conclusion that the aerosols production efficiency is *decreased* by the addition of surfactant. The approach by Prather *et al.* (2013) intends to bring the ocean, with all its complexity, into the laboratory, with controlled blooming experiment, along with carefully injected bubbles, to observe the associated aerosols production. In this case, the large variations of biological activity during the bloom went almost undetected in the sea spray properties (aerosols number and sizes). The problem is certainly complex, as even the major trends seem to remain not perfectly clear, and a physics-based parameterization is still to be unveiled. All three articles finally acknowledge and discuss the likely role of bubbles clustering in rafts, or whitecaps, but remain elusive about actual mechanisms (Modini *et al.* 2013), or applicability of very dense foams to oceanic conditions (Frossard *et al.* 2019). Numerous other studies have been performed (see for instance the introduction and comparison in Modini *et al.* (2013)) but the inclusion of a universal physico-chemical control on aerosol production remains an open question.

1.5. *A dedicated study on collective surface bubble dynamics in controlled conditions*

Therefore, on the one hand, individual bursting mechanisms have benefited over the years from detailed laboratory experiments, high-fidelity simulations and a comprehensive theoretical framework. On the other hand, intense research both on the physico-chemistry of interfaces and on the sea surface in the lab as well as in the field, have highlighted the critical role of surface-active material, whether biological (bio-film) or engineered (surfactants). In between, data that would embrace the full complexity of the problem are hard to acquire and to rationalize according to available physics-based parameterizations.

We are presenting a laboratory study aiming at filling this gap in knowledge, and attempt to quantify the role of collective effects from bubbles assembled at the surface of water. Two complementary set-ups are designed, that altogether fully characterize the dynamical and statistical evolution of bubbles at the surface of water. The experimental facilities allow for a careful control of the underwater bubble plume, characterized by its size distribution and density. Independently from the bubbles production, we investigate the role of water surface contamination by adding various concentrations of surfactant (sodium dodecyl sulfate and Triton X-100). We monitor the surface bubbles dynamics over time scales nearly covering the range highlighted in figure 1, short enough to capture their dynamics (down to 10 ms), as well as long enough (up to hours) to achieve and study converged statistics.

The paper is organized as follows. We depict the experimental set-ups in §2: a time-resolved bubble raft decay in §2.2, and a statistically stationary bubble plume in §2.3. The dynamics of the bubble raft for increasing levels of surface contamination are first analyzed in the freely decaying configuration in §3, from which global bubbles merging and bursting rates are measured for increasing surfactant concentrations. Next, the raft dynamics under a continuous injection of bubbles are described in §4, where we identify two regimes of collective surface bubbles evolution: one featuring relatively clean water, high probabilities of coalescence and short bubble lifetime, and another one with contaminated water, no coalescence and longer lifetime. We characterize the statistics of these regimes in §5. The findings are finally rationalized in a cellular automaton model in §6, before conclusions and recommendations are given in §7.

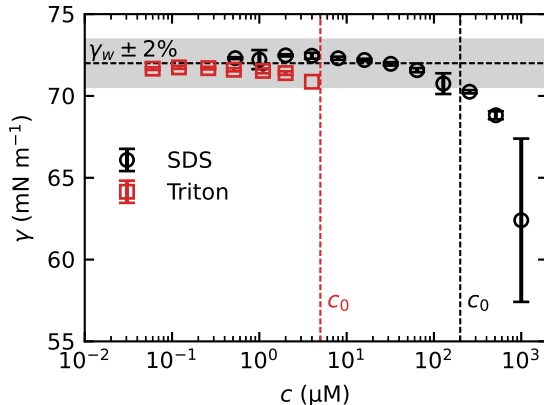


Figure 2: Static surface tension γ of solutions of sodium dodecyl sulfate (SDS, black, $CMC = 8.2$ mM) and Triton X-100 (Triton, red, $CMC = 220$ μ M) in deionized water, by the pendant drop method. The concentration c_0 indicates a departure of 2% from the value in pure water $\gamma_w = 72$ mN m^{-1} , highlighted by the shaded gray area.

2. Experimental set-ups

2.1. Surface contamination

We investigate and present in this article the role of surface contamination by the model surfactants sodium dodecyl sulfate (SDS, by Sigma-Aldrich) and Triton X-100 (Triton, by Sigma-Aldrich) on the behavior of the bubbles at the surface. SDS and Triton are chosen as common and well known, anionic and nonionic surfactants, respectively (Mysels 1986; Fainerman *et al.* 2009, 2010). Whether initially solid (SDS) or liquid (Triton), a controlled mass (precision 1 mg) of surfactant is dissolved into water, in concentrations c smaller than the critical micellar concentration (CMC): $c = 0.1 - 300$ $\mu\text{mol L}^{-1}$ (hereafter μM), with $CMC = 8.2$ mmol L^{-1} for SDS, and $c = 0.25 - 50$ μM with $CMC = 220$ μM for Triton. The large volume of water in the main set-up (at least 84 L, see section 2.3) allows for such low surfactant concentrations, and solutions for the raft decay experiment (described in section 2.2) were sampled *in situ*, scooping the required liquid quantity out of the bath surface. Deionized, clean water at room temperature was systematically used, and atmospheric conditions (temperature, humidity and pressure) frequently recorded in the course of the experimental runs.

Static surface tension $\gamma(c)$ is measured by the pendant drop method (Berry *et al.* 2015), with the results plotted with respect to the concentration c in surfactant in figure 2. Our values are consistent with data tabulated in the literature (Mysels 1986; Fainerman *et al.* 2009, 2010). However, note that the *static* surface tension is not the main control parameter in the context of the *dynamical* processes of bubbles merging and bursting at a free surface. Instead, we keep the surfactant concentration c as the experimental contamination parameter. In particular, below a certain concentration c_0 and within the pendant drop observation time (typically a few seconds to a few minutes), the static surface tension does not depart significantly from the clean water value $\gamma \simeq \gamma_w$ (for a departure of 2% from γ_w , $c_0 \approx 200$ μM for SDS, $c_0 \approx 5$ μM for Triton X-100). Most interesting behaviors, including the cancelling of coalescence probability between two bubbles (Yang & Maa 1984; Oolman & Blanch 1986; Shaw & Deike 2021), occur *below* that concentration. Above c_0 , γ eventually decreases within observable time (a few

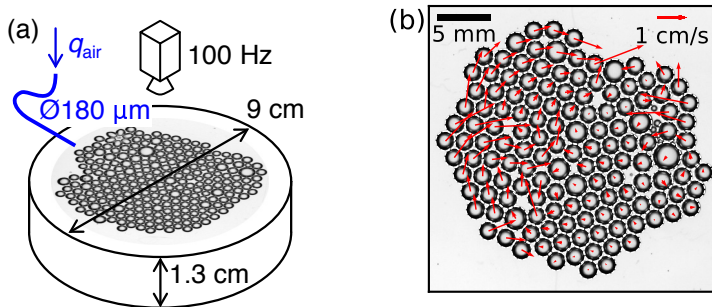


Figure 3: Bubbles raft decay experiment. (a) Monodisperse bubbles injected by blowing air through a needle. The needle is removed from the field of view prior to triggering images acquisition. (b) A sample image of a raft with $N = 149$ bubbles, shortly after the needle removal (SDS, $c = 256 \mu\text{M}$). Detected positions, sizes d_s (white dashed circles) and velocities (red arrows) are overlayed on top of the original image.

seconds), a signature of adsorption dynamics of surfactant molecules from the bulk to the surface, triggered by the increase in surface area when creating the pendant drop (Fainerman *et al.* 2009, 2010; Cantat *et al.* 2013).

2.2. Bubble raft decay

The first experiment, intended at characterizing bubble rafts dynamically, is shown schematically in figure 3. A raft of monodisperse bubbles is formed at the surface of a water bath by blowing air underwater at a controlled flow rate through a thin needle ($q_v = \mathcal{O}(5) \text{ cm}^3 \text{ s}^{-1}$, needle inner diameter $180 \mu\text{m}$). The level of water in the container (a Petri dish with diameter 9 cm and height 13 mm) is kept slightly above the dish edges, so that the concave meniscus prevents bubbles from accumulating on the sides. As seen on figure 3b, the typical bubble diameter $\langle d_b \rangle = 1.9 \pm 0.1 \text{ mm}$ lies in the millimetric range, and the raft extent does not exceed a third of the dish diameter. Potential influence from the container sides may therefore be safely neglected. For each solution, the experiment is repeated at least ten times under the same atmospheric conditions (temperature, relative humidity, pressure), with some variability in the number of initial bubbles N_0 . The mean bubble size $\langle d_b \rangle$ is not modified by the addition of surfactant (see also §2.3.2 and figure 6).

Images acquisition, from above, is triggered when the bubbling needle is removed from the bath (and off the field of view), at a frame rate of 100 Hz, or higher. The bath is illuminated from below with a uniform LED panel. On every frame, bubbles diameter d_s and x, y position on the water surface are detected unequivocally by intensity thresholding. Individual bubbles are then tracked across frames, giving access to their horizontal displacements and velocities (figure 3b).

In the course of a raft lifetime, bubbles do not only move at the surface, they may also merge, and they eventually burst. Coalescence events are tracked based on bubble volume conservation. At merging, two bubbles i, j with respective diameters d_i, d_j disappear into a newly formed bubble k , with diameter d_k . Bubbles are large enough to safely neglect the Laplace pressure contribution differential before and after the coalescence, and volumes d_s^3 (up to prefactors) add up: $d_k^3 = d_i^3 + d_j^3$ (see also section 2.3.1). Figure 4a depicts one example of a raft before and after a merging event, highlighting the bubbles involved in the process and the successful detection. Figure 4b reconstructs a 3-steps coalescence tree, leading to the formation of a bubble larger than the injected size

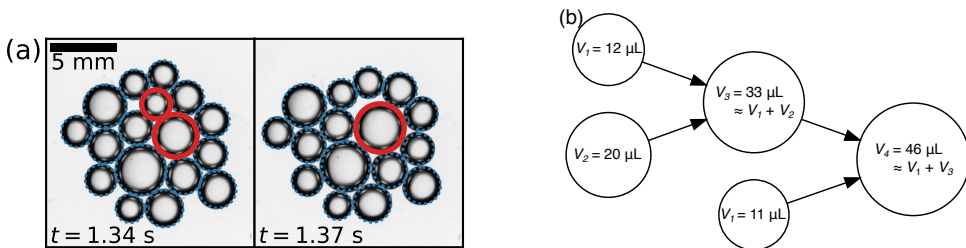


Figure 4: Bubbles coalescence detection. (a) A merging event detection is highlighted in thick red circles. (b). The tracking of merging events is illustrated in a 3-steps coalescence tree. The value of the bubble volume $V = d^3$ (μL) is indicated in each circle. It is, within an experimental error of a few percents, conserved during a merging event.

$\langle d_b \rangle$. This automated processing (bubble detection, tracking, and events characterization) allows to follow accurately the number of bubbles in the raft along time $N(t)$, and record the number of merging and bursting events $N_m(t)$ and $N_b(t)$, respectively.

2.3. Statistically stationary raft

2.3.1. Overall description

The following experimental set-up aims at creating an ensemble of bubbles of controlled sizes, with a fairly monodisperse distribution, and then monitoring their free evolution at the surface of a water bath. It is distinguished from the raft decay set-up described in the previous section 2.2 in that it involves a much larger number of bubbles, which are characterized in a statistically stationary fashion. Its primary constituent is a transparent acrylic tank with side 60 cm, filled with liquid up to 50 cm in height, open on the top as shown in figure 5. At the bottom is attached a pressurized, independent air chamber out of which needles, regularly spaced on a circle of diameter 15 cm, point vertically upwards in the tank. The projection of this circle onto the liquid-air interface, where bubbles produced at the bottom of the tank emerge, constitutes the outer edge of the monitored region. Different needles arrangements are used, with 16 to 48 identical needles in each case, with respective inner diameters 203 to 432 μm . The continuous and controlled injection of air inside the chamber, where the pressure is high and homogeneous, results in the regular formation of bubbles at the tip of every single needle, at a constant rate (Clift *et al.* (1978), Kulkarni & Joshi (2005)).

The air flow rate blown in the pressurized chamber is a second parameter which is systematically varied, from 0.5 L min^{-1} for all needles to equally bubble, up to 20 L min^{-1} (flow controller Alicat Scientific MCS). It sets, jointly with the needles size, the bubbles plume various parameters: bubbles sizes d_b in the bulk, number $n_b(d_b)$ per unit volume and production rate p_b . The volume flow rate q_v , automated as a set point for the whole pressurized chamber, is given per needle. Corresponding mass flow rate, temperature and pressure are frequently recorded.

At the surface, the total area available to bubbles is maximal at 36 dm^2 (*i.e.* the horizontal tank cross section). In order to limit the surface bubbles drifting motion, we also performed experiments restricting this area available to bubbles, down to a few dm^2 , by placing floating boundaries between the tank walls and the bubbles emerging region. As will be seen in section 5, the modified available area did not affect sensibly the statistical response of the surface bubbles.

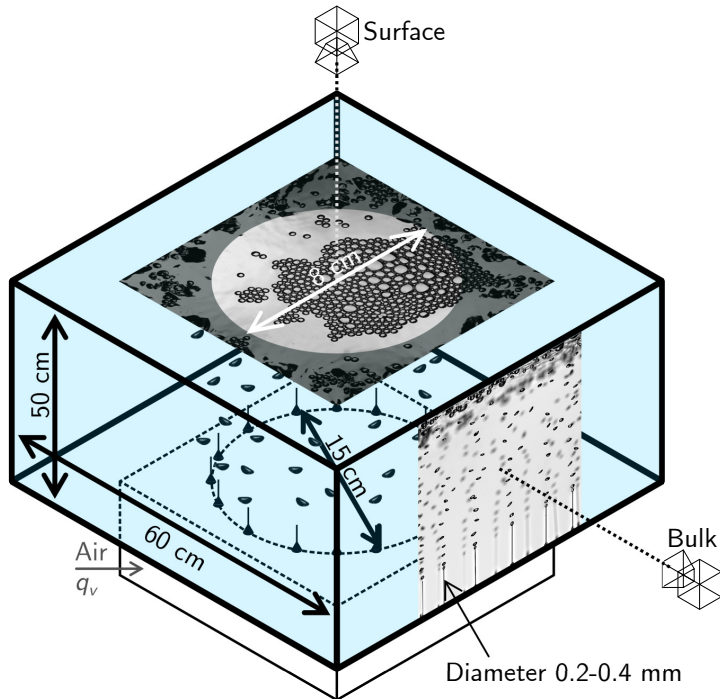


Figure 5: Statistically stationary experiment. A pressurized chamber, located underneath a tank filled up with water, is fed with air at a constant flow rate q_v to produce bubbles through needles pointing upwards into the tank (dimensions $60 \times 60 \times 50 \text{ cm}^3$). The bubbles at the surface (respectively in the bulk) are monitored inside their emerging area, thanks to a camera placed above the surface, looking down at it (resp. on its side, looking at one needles' plane in the bulk). The inserted, magnified views are typical raw frames grabbed from the corresponding top and side cameras.

2.3.2. Bulk bubbles

Air bubbles in the bulk are produced at the needles tip at the bottom of the tank and then rise to the surface thanks to buoyancy. The overall bulk bubbles statistics are measured over a representative subset of needles, by means of a camera located on the side of the tank (Basler acA1440-220um), with a typical resolution of $50 \mu\text{m}$ per pixel. The acquisition framerate, 2 Hz , is chosen to be slower than the inverse of the transit time of a bubble across the observed height (10 cm to be divided by a typical rising velocity 30 cm s^{-1} is 0.3 s), ensuring successive frames independence. A higher frame rate was also used to monitor the bubbles rising dynamics. Statistics are performed over around 1,000 bubbles, gathered from at least 10 independent images, achieving statistical convergence.

After a transient straight rise, the millimetric bubbles trajectories destabilize to follow an upward oscillatory, helical path (Saffman 1956; Duineveld 1995; Mougin & Magnaudet 2002; Cano-Lozano *et al.* 2016). The spacing between the needles, about 3 cm , is of the same order of magnitude as the peak-to-peak amplitude of the trajectory oscillation, so that the bubbles paths are either close to overlap, or do so slightly. In the latter case, no coalescence was observed before the bubbles reach the liquid-air interface. Measuring the typical vertical separation between bubbles (about 7 mm), an estimate for the volume of the cylinder available to every single bubble before seeing a neighboring one is

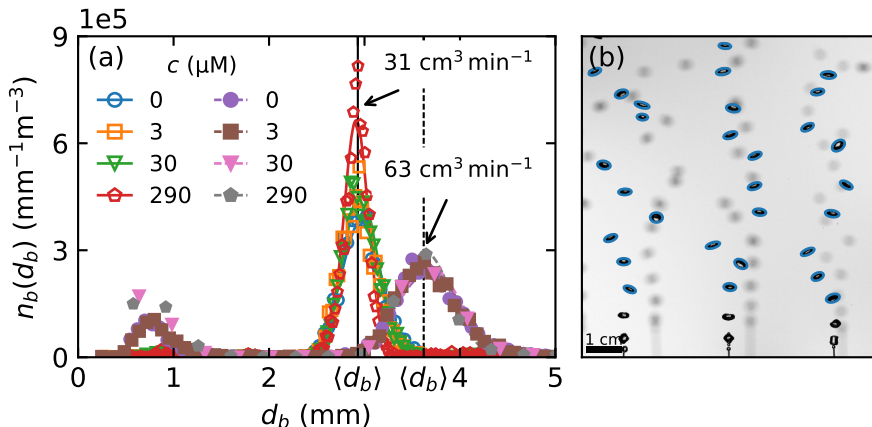


Figure 6: (a) Size distribution $n_b(d_b)$ of bubbles in the bulk, per unit volume, for 4 SDS concentration ($c = 0, 3, 30$ and 290 μM , different symbols) and 2 air flow rates ($q_v = 31$ and 63 $\text{cm}^3 \text{min}^{-1}$ per needle, respectively hollow and filled markers). The lines are the best gaussian fits for the main peak $\langle d_b \rangle \approx 3 - 4$ mm. At high flow rates, smaller bubbles ($d_b \approx 0.8$ mm) are produced and the statistics depart from strictly gaussian to bimodal, with a secondary peak close to 0.8mm. (b) Raw still image from the side camera showing 3 needles (inner diameter 203 μm) producing bubbles. Fitted ellipses are overlayed on top of the detected bubbles, characterized by their volume-equivalent diameter d_b (case $q_v = 31$ $\text{cm}^3 \text{min}^{-1}$, $c = 0$ μM).

$0.7 \times 3^2 \pi / 4 = 5$ mL. The void fraction finally divides the bubble volume itself (typically 10 μL) by this surrounding water volume, to range in a dilute regime (0.1-0.2%).

Figure 6a shows the bulk bubble size d_b distribution $n_b(d_b)$ for two flow rates $q_v = 31$ and 63 $\text{cm}^3 \text{min}^{-1}$ and four SDS concentrations $c = 0, 3, 30$ and 290 μM . Bubbles edges are automatically detected by way of image processing, and fitted onto ellipses with major and minor axes a and b , respectively (an example for the bubbles detection is plotted in figure 6b). Their size is computed as the volume-equivalent diameter $d_b = \sqrt[3]{a^2 b}$, assuming the axi-symmetry of the bubbles around the fitted ellipse minor axis b .

The distributions presented in figure 6a draw three trends:

- First, the bulk bubbles distributions are bimodal, with two distinct peaks. A principal gaussian peak is unambiguously defined at all flow rates, which defines the mean bulk bubble size $\langle d_b \rangle$. For low and moderate flow rates, it aggregates the vast majority of bubbles and will be the main point of interest throughout this article. We acknowledge the existence of a secondary peak, especially visible for higher flow rates (around $d_b \approx 0.8$ mm for $q_v = 63$ $\text{cm}^3 \text{min}^{-1}$ in figure 6a), made of smaller, sub-millimetric bubbles. They are generated as daughters of the main bubbles in the pinch-off process, due to high air velocities and irregular air extraction at the needle tip.
- Second, the comparison between the two air flow rates in figure 6a highlights the control over the mean bulk size $\langle d_b \rangle$ by q_v , a higher flow rate producing bigger bubbles, with broader dispersion around the mean size ($\langle d_b \rangle = 2.9 \pm 0.2$ mm at $q_v = 31$ $\text{cm}^3 \text{min}^{-1}$, against $\langle d_b \rangle = 3.6 \pm 0.3$ mm at $q_v = 63$ $\text{cm}^3 \text{min}^{-1}$).
- Finally, variations of the SDS concentration c over several orders of magnitude have no influence on the bulk bubbles mean size $\langle d_b \rangle$, though it is known to modify its shape (Magnaudet & Eames 2000; Zenit & Magnaudet 2008) and rise velocity (Clift *et al.* 1978).

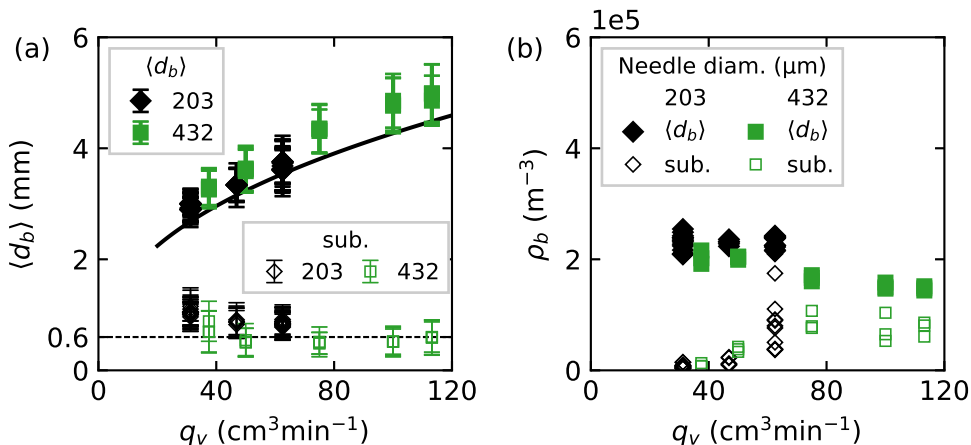


Figure 7: Bulk bubbles properties as a function of the flow rate q_v , for two different needle diameters (black diamonds: 203 μ m and green squares: 432 μ m). (a) Bulk bubble mean size $\langle d_b \rangle$ (filled symbols) and secondary sub-millimetric peak (hollow thin markers). Error bars quantify the standard deviation of the gaussian kernel around $\langle d_b \rangle$. The dark line is equation (2.1). (b) Bubbles bulk density $\rho_b = \int n_b(d_b)dd_b$ around $\langle d_b \rangle$ (filled markers) and in the secondary sub-millimetric peak (hollow thin markers). SDS concentration is not represented since no trend can be drawn, but is accounted for some scatter in the data at a constant flow rate.

These trends are confirmed in figure 7. Figure 7a shows both the bubbles mean size $\langle d_b \rangle$ and average diameter of the secondary sub-millimetric bubbles as a function of the flow rate q_v , for all SDS concentrations and two needles sizes used. As the flow rate per needle is increased from 20 to 120 cm³ min⁻¹, the bulk bubble size $\langle d_b \rangle$ increases from 3 to 5 mm, with little influence from the needle diameter or the SDS concentration. The evolution is well captured by the equation proposed by Davidson & Schüller (1960) (fig. 7a, solid line) for bubbles forming from a single orifice in an inviscid liquid:

$$\langle d_b \rangle = \left(\frac{6 \times 1.378}{\pi} \right)^{1/3} q_v^{2/5} g^{-1/5}. \quad (2.1)$$

In the same time, the sub-millimetric bubbles sizes slightly decrease as the flow rate is increased over the same range.

Figure 7b shows the bulk density of bubbles in the water column, $\rho_b = \int n_b(d_b)dd_b$, as a function of the flow rate, for the two needle diameters being used (203 and 432 μ m). Again, the contributions for the main mode around $\langle d_b \rangle$ and the sub-millimetric bubbles are separated. Around $\langle d_b \rangle$, the bubbles number ρ_b slowly decreases from 2×10^5 to 1.5×10^5 m⁻³, at all surfactant concentrations and for both needle sizes, indistinctly. On the contrary, the number of sub-millimetric bubbles is strongly affected by the needles size. For the same flow rate, the smaller the needle inner diameter, the higher the air velocity in the needle, disturbing greatly the pinch-off at the needle tip. With the smallest needle (inner diameter 203 μ m) at highest flow rate (120 cm³ s⁻¹), we generously estimate an incompressible air velocity of 60 m s⁻¹, whose magnitude may suffice to explain the irregular daughter bubbles formation that can then occur. In the following, we are focusing on results where the production of sub-millimetric bubbles is negligible (*i.e.* moderate flow rates).

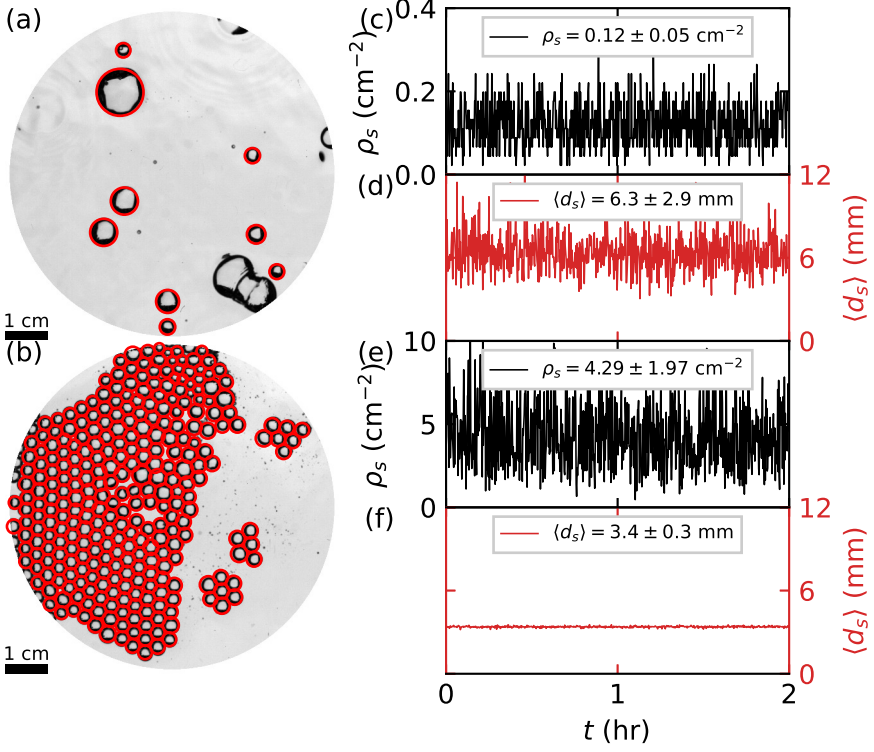


Figure 8: Two experiments for the same flow rate $q_v = 47 \text{ cm}^3 \text{ min}^{-1}$ and two different SDS concentrations: (a, c, d) $c = 1 \text{ } \mu\text{M}$ (traces) and (b, e, f) $c = 92 \text{ } \mu\text{M}$ (enough surfactant to prevent coalescence). (a, b) Bubbles detection at the surface from typical frames. (c, e) Bubbles surface density ρ_s (number of bubbles on each frame divided by the surface area, black). The case with traces of surfactants features a density almost 40 times smaller than the case with more surfactants, with similarly high variability ($\rho_s = 0.12 \pm 0.05$ and $4.29 \pm 1.97 \text{ cm}^{-2}$, respectively). (d, f) Bubbles diameter averaged over each frame $\langle d_s \rangle$ (red). With more surfactant and for the same bulk bubble size, both the surface bubble mean size and variability are reduced ($\langle d_s \rangle = 6.3 \pm 2.9$ and $3.4 \pm 0.3 \text{ mm}$, respectively).

The total production rate of bubbles in the bulk is $p_b = N_{\text{needles}} f$, with N_{needles} the number of needles and $f = q_v / (\pi \langle d_b \rangle^3 / 6)$ the bubbling frequency at each needle tip. f is eliminated using equation (2.1), and we can write:

$$p_b = 0.726 N_{\text{needles}} q_v^{-1/5} g^{3/5}. \quad (2.2)$$

Note that p_b decreases slowly with the flow rate q_v , a direct consequence of the increase of the bubble volume $\langle d_b \rangle^3 \propto q_v^{6/5}$ (eq. 2.1), slightly faster than q_v . p_b typically ranges around 500-1,000 bubbles produced per second in the bulk.

2.3.3. Surface bubbles

We are ultimately interested in the statistical behavior of the bubbles at the surface. A top view camera (Basler acA2040-90) records the surface bubbles evolution over time, with a resolution of $50 \text{ } \mu\text{m}$ per pixel. The frame rate (1 image every 10 or 30 s) is

chosen slower than all bubble typical time scales (discussed in §1) so as to ensure frames statistical independence, while higher frame rate measurements will be discussed in §4.

The observation and subsequent analysis are restricted to the disk region inside the bulk bubbles surfacing rim (diameter 8 cm), where visualisation is clear of any disturbance of the liquid-air interface and surface bubble identification straightforward. Figures 8a and b show two examples of such observations at different surfactant concentrations (but the same flow rate), along with the bubbles detection (location and size). Bubbles edges are uniquely detected by thresholding the gray-levels images, and identified by their area-equivalent diameter d_s , as seen from the top (further technical details are given in appendix A).

The present experimental geometry is successful in studying accurately the surface bubbles without effect of the sides of the container: bulk bubbles emerge at the surface into a rim, and surface bubbles are observed inside that rim. Note that not all bubbles produced in the bulk make their way into the imaged area: roughly half of them emerge on the outer side of the rim, and another fraction merge and/or burst before reaching the region of interest. We quantify the proportion of bubbles reaching the region of interest by introducing an *ad hoc* non-dimensional ratio α , measured on selected cases thanks to time-resolved measurements (83 Hz), and estimated for the general case between 1/10 and 1/2. The surface bubbles production rate p_s is then:

$$p_s = \alpha p_b . \quad (2.3)$$

The continuous and radial influx of bubbles into the imaging area, surrounded by the rim of bubbling needles, makes it very unlikely that surface bubbles exit the region of interest before bursting, and such rare events are not considered.

Figures 8c-f show extended time series for the bubbles density at the surface ρ_s and their mean size $\langle d_s \rangle$, for the corresponding cases (fig. 8a, b). They demonstrate the statistical stationarity of the setup on such long time scales, with a well defined mean density with large fluctuations, as well as a well defined mean bubble size. The variability in fluctuations depends on the level of contamination, and is characteristic of two different regimes, studied in great details in section 4:

- a *clean water regime*, or with traces of surfactants, which features a low bubbles surface density and large variabilities in the bubble sizes and surface density ($\rho_s = 0.12 \pm 0.05 \text{ cm}^{-2}$, $\langle d_s \rangle = 6.3 \pm 2.9 \text{ mm}$, figure 8a, c, d). The broad range of bubble sizes at the surface comes necessarily from coalescence at the surface since we have seen in section 2.3.2 that our initial bulk bubble size distribution is much narrower;
- a *contaminated regime*, where the addition of surfactants above a certain threshold (which will be discussed below and relates to the ability for bubbles to coalesce) suppresses the variability for the bubbles mean size ($\langle d_s \rangle = 3.4 \pm 0.3 \text{ mm}$, fig. 8f). The surface density mean value is increased by a large factor when compared to the clean water regime, while preserving an important variability over time ($\rho_s = 4.3 \pm 2.0 \text{ cm}^{-2}$, fig. 8e). Bubbles cluster in rafts, as seen in figure 8b, which remain monolayers for the parameters we use.

The surface bubbles are identified by their apparent diameter d_s measured from the top, as shown in figure 8a, b, from which we will compute their volume. Yet, in both regimes, bubbles at the surface have a diameter which is comparable to the capillary length $\ell_c = \sqrt{\gamma/\rho g}$ ($= 2.7 \text{ mm}$ for clean water. At higher concentrations of surfactant, γ and hence ℓ_c are not sensibly modified, see figure 2). In other words, bubbles at the surface are neither quite spherical (which would require $d_s \ll \ell_c$), nor hemi-spherical ($d_s \gg \ell_c$), as illustrated by the theoretical bubble profiles in figure 9a-c. Therefore, we calibrate the surface bubble volume in this intermediate regime as a function of the non-

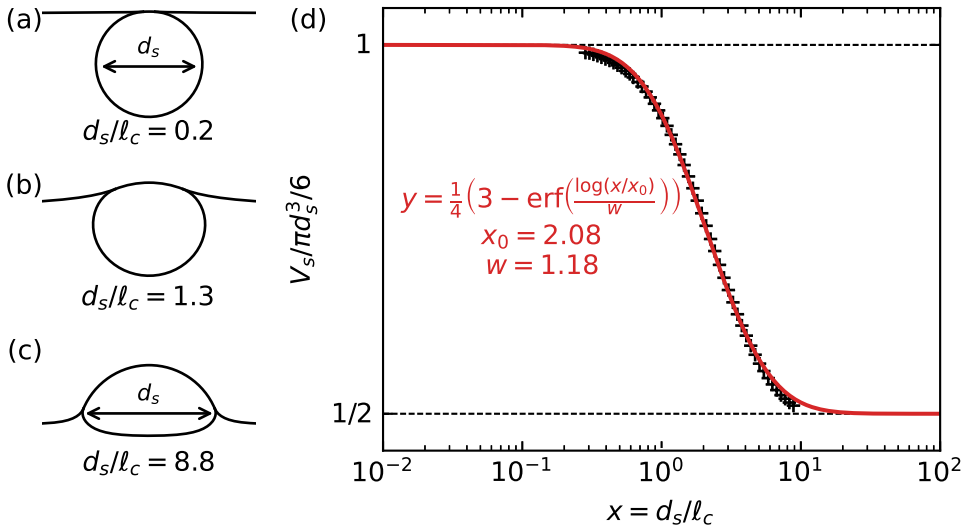


Figure 9: Surface bubble volume calibration. (a – c) Profiles of a single static bubble at the surface of liquid, solving the Young-Laplace equation for $d_s/\ell_c = 0.2, 1.3$ and 8.8 respectively. (d) Bubble volume V_s , normalized by the equivalent sphere volume $\pi d_s^3/6$, as a function of $x = d_s/\ell_c$ (black markers) and best fit of error function $y = \frac{1}{4} \left(3 - \text{erf} \left(\frac{\log(x/x_0)}{w} \right) \right)$ over the offset x_0 and width w for the transition cases (red line).

dimensional surface bubble diameter $x = d_s/\ell_c$ ($x = \sqrt{Bo}$ is the square-root of the Bond number Bo used in other contexts, with Bo between 0.8 and 2) by solving the Young-Laplace equation for a variety of single static bubbles in this regime (Toba 1959; Princen 1963; Berny *et al.* 2020). Figure 9a-c exhibits solved bubble profiles in this transition from submerged spheres to emerged half-spheres. Figure 9d then plots the normalized volume $V_s/(\pi d_s^3/6)$, computed from the solution profiles, as a function of the non-dimensional diameter x . Alongside is plotted the appropriate error function which satisfies both the small x (submerged, spherical bubble) and large x (emerged, hemispherical bubble), and whose offset x_0 and width w fit best the volume data in the step between asymptotics. Note that the choice of the error function is a convenient fit but other functional form could have been chosen. This calibration allows to go from bubble volume measured in the bulk to the corresponding bubble volume at the surface.

3. Dynamics of decaying rafts

The dynamics of surface bubble rafts are first studied in a freely decaying experiment, where an initial ensemble of air bubbles N_0 is let free to evolve at the surface of water, namely to move, coalesce and burst.

3.1. Exponential decay

Once they are formed, the initial N_0 bubbles in the raft start to merge and burst and their number N decreases with time t (see experimental details in §2.2). Figure 10 illustrates the decay of the number of bubbles $N(t)$ in the raft for multiple initializations N_0 at the same SDS concentration $c = 256 \mu\text{M}$ (all other experimental conditions are kept the same: bubbles production, needle, temperature, air humidity, atmospheric

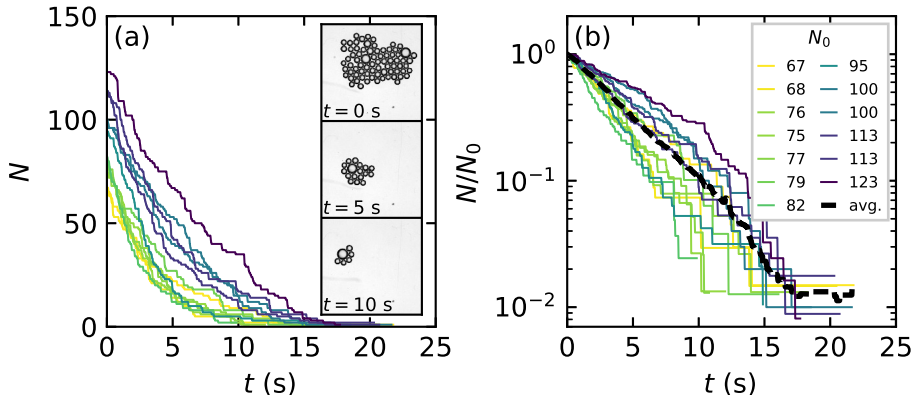


Figure 10: Time evolution of the number of bubbles in the raft $N(t)$ (SDS, $c = 256 \mu\text{M}$). (a) Multiple runs under the same experimental conditions (bubble production, atmospheric conditions), for different raft initializations N_0 . (b) The same data is normalized by N_0 and shown in logarithmic scale. The thick dashed black line is an ensemble average on all realizations.

pressure, etc.). As better seen in logarithmic scale, the decay can be described by a decreasing exponential (figure 10b):

$$N(t) = N_0 e^{-t/\tau_r}, \quad (3.1)$$

where the constant τ_r is the raft decay time, or half-life. Expression (3.1) is the signature of a proportionality between the bubbles disappearing rate $\dot{N}(t)$ and $N(t)$, which is discussed in §3.2. Despite a large variability in the raft initializations, one can not observe an influence of N_0 on the raft decay: the colors in figure 10b exhibit no specific ordering or pattern. Eventually, the exponential decay is best appreciated when considering an *ensemble-averaged* bubbles number, over all raft realizations (thick dashed black line in figure 10b).

We measure the raft decay time τ_r as the single parameter in equation (3.1), fitted on experimental $N(t)/N_0$ data. It is a global measure of the raft, averaging and smoothing out the spatial and temporal details (deviations to a strict exponential decay, influence of edges, and other potential effects that are neglected in the following). Figure 11 plots τ_r as a function of the surfactant concentration for SDS and Triton X-100 (fig. 11a and b, respectively). The variability observed in figure 10b is visible at all concentrations, independent of N_0 (displayed in different colors). It is made visible in the large error bars around the values averaged over each surfactant concentration (black empty squares).

The evolution of τ_r with the surfactant concentration c exhibits a complex behavior. At high surfactant concentrations and for both surfactants, the increase of τ_r with c is clear, and in agreement with the increase of individual bubble lifetimes with surface contamination (Garrett 1967; Champougny *et al.* 2016; Atasi *et al.* 2020), along with the fact that bubbles lose their ability to coalesce (Oolman & Blanch 1986; Langevin & Rio 2015). Decreasing c from the high concentration cases, the decay time τ_r seems to reach a local maximum, or at least a plateau, before slowly evolving towards what would be the value extrapolated for clean water. However, for very low concentrations, almost traces of surfactant, it becomes increasingly difficult to form rafts, as bubbles merge almost

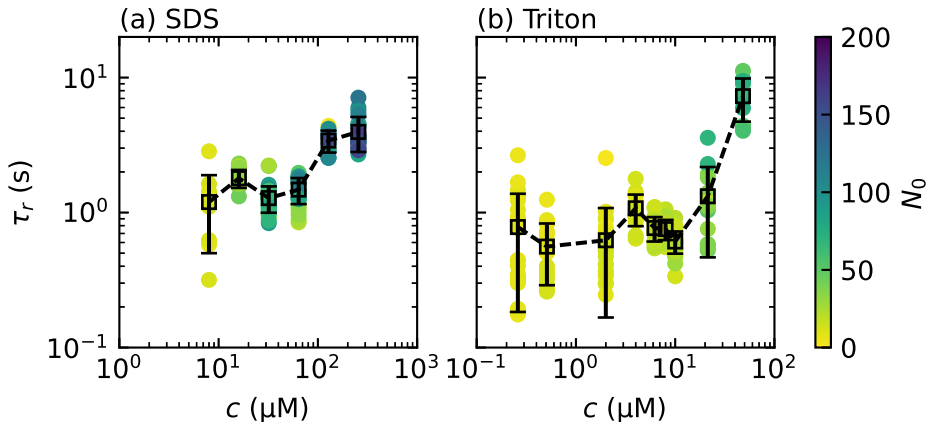


Figure 11: Exponential decay time τ_r as a function of the surfactant concentration c for (a) SDS and (b) Triton X-100. Each circle represents a raft, with color coding the initial number of bubbles N_0 . Black empty squares are averaged values for each concentration, error bars indicating standard deviation. Dashed lines are a guide to the eyes.

instantly and burst rapidly. This non-trivial behavior is rationalized by studying more closely merging and bursting events during the raft decay.

3.2. Bursting and merging rates

Initiated with a number $N(t=0) = N_0$, the number of bubbles $N(t)$ in a raft decreases with time, due to increasing numbers of bubbles *merging events* $N_m(t)$ and number of bubbles bursting $N_b(t)$:

$$N(t) = N_0 - N_m(t) - N_b(t) . \quad (3.2)$$

The merging rate \dot{N}_m is the number of bubbles merging per unit time (respectively \dot{N}_b for bubbles bursting). It is a quantity proportional to the current number of bubbles in the raft $N(t)$ at any time:

$$\dot{N}_m = q_m N(t) , \quad \dot{N}_b = q_b N(t) \quad (3.3)$$

where the global rates, or frequencies, q_m, q_b are inferred constant. Deriving and solving (3.2) retrieves the exponential decay (3.1) and gives τ_r as a function of q_m and q_b :

$$\frac{1}{\tau_r} \equiv q_r = q_m + q_b . \quad (3.4)$$

We define $q_r = 1/\tau_r$ as the global raft decay rate, and is used interchangeably with τ_r in what follows. Equations (3.3) are finally solved with $N_m(0) = N_b(0) = 0$ and the numbers of bubbles merging and bursting read:

$$\frac{N_m(t)}{N_0} = q_m \tau_r \left(1 - e^{-t/\tau_r} \right) , \quad (3.5)$$

$$\frac{N_b(t)}{N_0} = q_b \tau_r \left(1 - e^{-t/\tau_r} \right) . \quad (3.6)$$

Figure 12 presents experimental time series of the different bubble counts $(N(t), N_m(t), N_b(t))$ for rafts at three increasing surface concentrations (SDS at $c = 8, 16, 256$ μM , respectively). These three cases already define two asymptotic

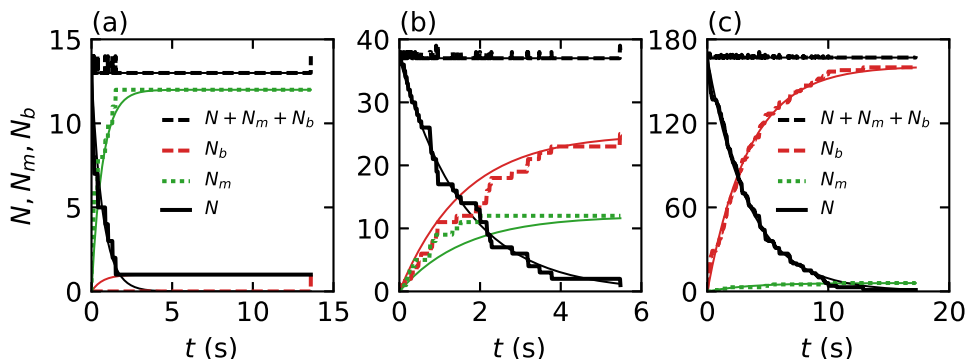


Figure 12: Bubble counts along time, in rafts with SDS at concentrations (a) $c = 8 \mu\text{M}$, (b) $c = 16 \mu\text{M}$ and (c) $c = 256 \mu\text{M}$. N total count (solid black line), N_m cumulative number of merging events (dotted green line), N_b cumulative number of bursting bubbles (dashed red line) and summation $N + N_b + N_m$ (dashed black line, equating N_0). Thin lines are respective equations (3.1), (3.5) and (3.6), with τ_r adjusted and q_m, q_b given by (3.7).

regimes (low and high contaminations) and the transition between the two, as will be further discussed in the next section. At low surfactant concentration (fig. 12a), bubbles in the vicinity of one another attract by meniscii interactions but can not stay close for a long amount of time: they coalesce as soon as they touch. As a consequence, merging dominates over bursting $N_m(t) \gg N_b(t)$. Specifically, figure 12a represents a limit case, where $N_b(t) = 0$ up until the very end of the raft, *i.e.* only the last bubble of the raft bursts, being the result of the merging of all other bubbles. At high surfactant concentrations (fig. 12c), bubbles still attract each other by way of capillarity, but now coalescence is greatly reduced and they can stay close to each other, for extended amounts of time. Merging is then marginal, and the dynamics of the raft is dominated by bursting: $N_b(t) \gg N_m(t)$. The limit case mirroring the low contamination one is when no bubbles are merging, or $N_m(t) = 0$ at all time t . At intermediate concentration (fig. 12b), bubbles merge and burst in comparable proportions $N_m(t) \sim N_b(t)$. The crossover between the two asymptotic regimes will uniquely define a transition concentration c_* (see §3.3 below and figure 14).

This knowledge of all merging and bursting events in the lifetime of a raft directly gives access to the merging and bursting rates q_m and q_b , respectively. For a raft of bubbles, $\tau_r = 1/q_r$ first needs to be measured, by fitting equation (3.1) on experimental data $N(t)$ (N_0 being imposed by the data, τ_r is the only free parameter). Then equations (3.5) and (3.6) are estimated at $t = +\infty$, that is the end of the raft or bursting of its last bubble, to immediately give q_m and q_b :

$$q_m = \frac{N_m(+\infty)}{N_0} q_r, \quad q_b = \frac{N_b(+\infty)}{N_0} q_r. \quad (3.7)$$

Along with the experimental data for $N(t)$, $N_m(t)$ and $N_b(t)$, we plot on figure 12 the respective equations (3.1), (3.5) and (3.6), where the unknown rates are either adjusted (q_r) or calculated (q_m, q_b) as just described. The agreement is excellent, even in the case of rafts with a low number of bubbles, where the discrete nature of the bubble counts is a known limitation.

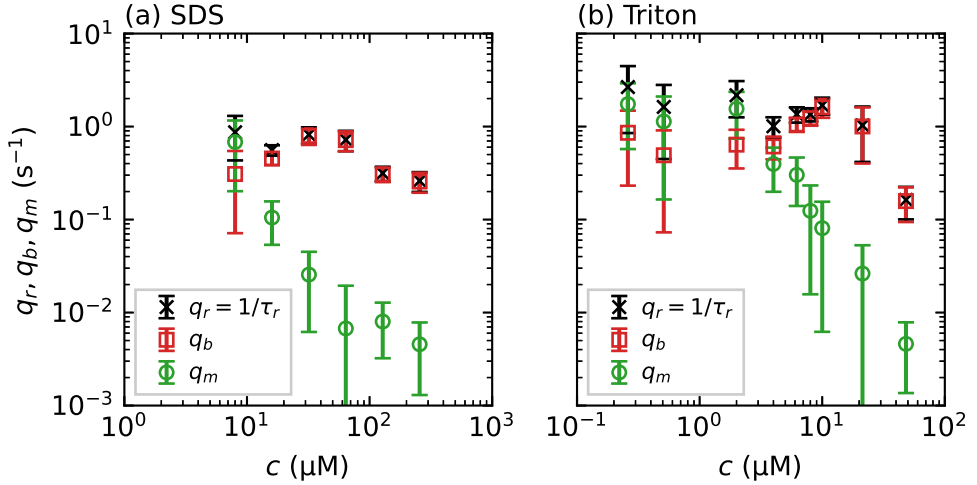


Figure 13: Decay rate $q_r = 1/\tau_r$ (result of the fit of $N(t)/N_0$ on equation (3.1)), and merging and bursting rates q_m, q_b (equation (3.7)), as a function of surfactant concentration c , for (a) SDS and (b) Triton X-100. Each point averages at least 10 raft realizations under the same bubble production and atmospheric conditions, and the error bar stands for the standard deviation.

3.3. Role of surfactants

The amount of surfactants in the liquid determines the raft behavior in a non-trivial way, as already shown on the global decay time τ_r (fig. 11). The differentiation between global merging and bursting rates q_m, q_b , allows to refine the analysis. Figure 13 gives these rates q_r, q_m and q_b as a function of the surfactant concentration c for SDS (fig. 13a) and Triton X-100 (fig. 13b). Each point is averaged over multiple raft realizations (at least 10), all acquired under the same atmospheric conditions and bubbles production. The regimes of low, intermediate and high contaminations, described above (see figure 12), are immediately identified and retrieved. At low concentrations, merging and bursting rates are approximately constant when c is varied, and merging dominates over bursting $q_m \gg q_b$. The merging rate $q_m(c)$ then transitions and starts to decrease, becoming of the same order of magnitude as q_b and then dropping to 0. Conversely, the bursting rate $q_b(c)$ increases slightly to reach a local maximum or plateau, before decreasing at higher values of concentration, where it dominates over merging $q_b \gg q_m$. By equation (3.4) $q_r = q_m + q_b$, bursting thus contributes primarily, at high concentration of surfactant, to the non-monotonic evolution already observed on τ_r (fig. 11).

Figure 14 eventually compares both surfactants SDS and Triton X-100. The evolution of the ratio of merging to bursting rates q_m/q_b is first plotted in figure 14a. It now defines formally the transition concentration c_* as the crossover between the coalescence-dominated regime (low contamination) and the bursting-dominated regime (high contamination). By taking $q_m/q_b|_{c=c_*} = 1$, we measure $c_* = 12 \mu\text{M}$ for SDS and $c_* = 4 \mu\text{M}$ for Triton X-100. Once normalized by c_* , as is the case in figure 14a, the evolution of q_m/q_b as a function of c/c_* is similar for both surfactants SDS and Triton.

In figure 14b, merging and bursting rates are compared to $q_* = q_r(c_*)$, the value of the raft decay rate at the transition concentration ($q_* = 0.2 \text{ s}^{-1}$ for SDS, $q_* = 0.4 \text{ s}^{-1}$ for Triton X-100). Remarkably, it collapses on a single plot the two features previously

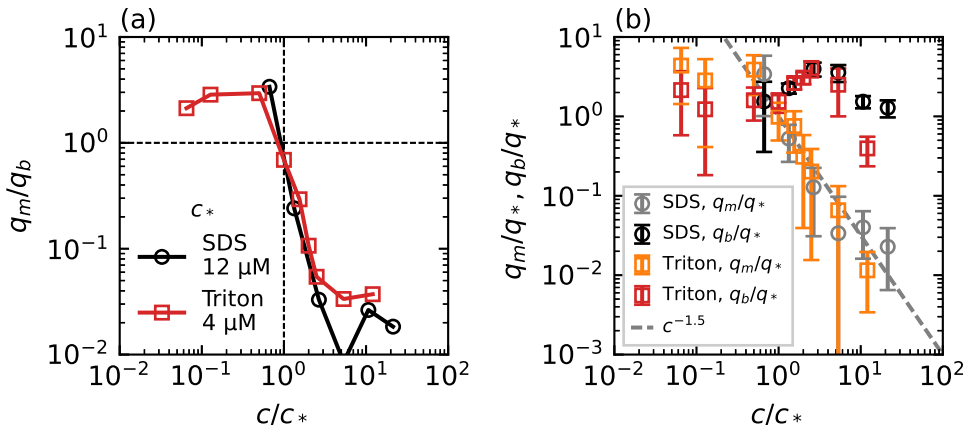


Figure 14: (a) Merging to bursting rates ratio q_m/q_b as a function of the normalized surfactant concentration c/c_* , for SDS and Triton X-100. c_* is defined as the transition concentration where $q_m = q_b$: $c_* = 12 \mu\text{M}$ for SDS, $c_* = 4 \mu\text{M}$ for Triton X-100. (b) Normalized merging and bursting rates q_m/q_* , q_b/q_* as a function of c/c_* for the two surfactants. q_* is defined as $q_* = q_r(c_*)$: $q_* = 0.2 \text{ s}^{-1}$ for SDS, $q_* = 0.4 \text{ s}^{-1}$ for Triton X-100. Above the coalescence transition $c \geq c_*$, the merging rate is well described by a power-law decay $q_m \propto c^{-\beta}$, with $\beta = 1.5$.

observed on both surfactants. On the one hand, the merging rate $q_m(c)$ vanishes after $c \geq c_*$, in a trend that is well described by a power-law $q_m \propto c^{-\beta}$, with $\beta = 1.5$ (note that we do not provide a theoretical argument to explain this evolution). On the other hand, the bursting rate $q_b(c)$ undergoes a short transitional increase for concentrations around and slightly above c_* , before dropping to 0. Lastly, this decoupling of merging and bursting rates with respect to the surfactant concentration, understood as a seemingly common feature across different surfactants, will guide choices of numerical parameters in section 6.

4. Statically stationary rafts: dynamics

The dynamics of bubble rafts at the free surface in the statistically stationary setup is now discussed phenomenologically. We observe two asymptotic regimes: i) in conditions close to clean water, where bubbles coalescence is possible, we observe a dilute regime with a broad distribution of sizes; ii) with enough surfactant, *i.e.* above the identified transition $c > c_*$, we observe a more mono-disperse collection of bubbles at the surface, clustering and forming long-living rafts.

4.1. Dilute regime in presence of coalescence

A relatively fast frame rate (83 Hz) is used to gain insight on the surface bubbles dynamics and typical time scales. Figure 15 shows a sequence of 3 seconds of typical bubbles activity at the surface of clean water (fig. 15a), and associated, singularized events (fig. 15b-f). A primary observation is that only a small fraction of the emerging bubbles (about 10 out of 500 to 1,000 per second) make their way into the region of interest. There, these are entrained towards the center of the region at velocities up to

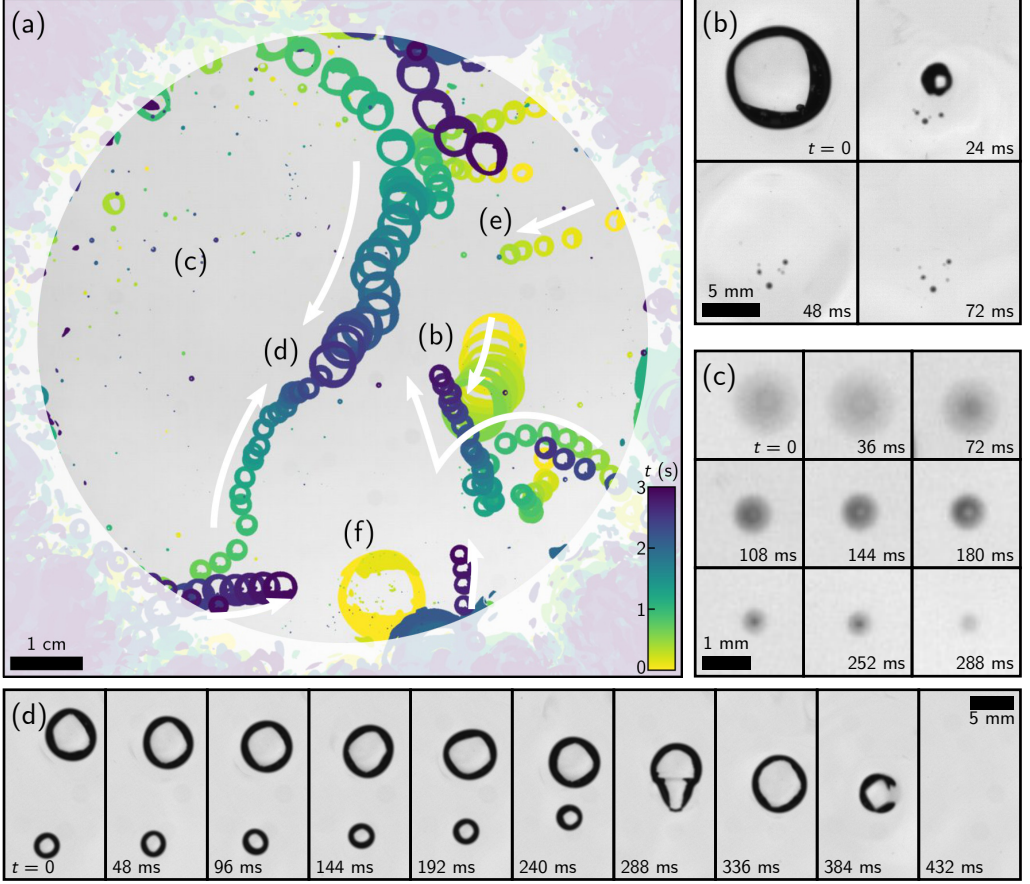


Figure 15: (a) 3 seconds of typical bubbles activity at the surface of clean water, with 690 bubbles being produced per second in the bulk. The sequence is recorded at 10.4 Hz and stacked with the minimum value of each pixel over time, colored with respect to time. White arrows indicate the general direction of motion for the nearest bubbles. The outer surfacing area is shaded. (b) A bubble bursting event, generating small bubbles from the retraction of the cap. Frames read from left to right, then top to bottom, separated by $\Delta t = 24$ ms. (c) A drop, initially out of focus, falls back on the bath and rebounds, losing mass. $\Delta t = 36$ ms. (d) A merging event, rapidly followed by a burst. $\Delta t = 48$ ms, rotated from (a). (e) A bubble emerging in the surfacing area and moving in the monitored region. (f) A bubble nearly 100 times as big as the injected individual volume.

0.1 m s^{-1} by the surface part of a large recirculation flow (fig. 15d, e). The latter is itself driven by the bubbles rising in the bulk, with an upwards velocity of about 0.3 m s^{-1} .

The lifetime of surface bubbles in still clean water is known to be a quantity highly sensitive to the environment (surface contamination by air-borne pollutants, water temperature, air humidity, etc.). As a result and even in the case of very careful experiments, it is broadly distributed, with values ranging from 0.1 to 10 s for centimetric bubbles (Zheng *et al.* 1983; Poulain *et al.* 2018). From the long time series, as the one presented in figure 15a, we observe a similar variability, from bubbles newly merged that burst within a few tens of milliseconds (fig. 15d, last four frames), to long-living bubbles that can travel around and cross the central region undisturbed (fig. 15a, d). Indeed, this time

scale $\mathcal{O}(0.1 - 1 \text{ s})$ compares well with the transport time of such bubbles across the central region (with diameter of around 0.1 m , to be divided by the typical velocity 0.1 m s^{-1}), allowing them to come into close proximity with other bubbles, and coalesce (fig. 15d). With clean water, coalescence is inevitable: once two bubbles touch, they merge, with a coalescence time scale from contact to full shape recovery of about 0.1 s . The multiple and successive coalescence processes allow to form bubbles up to 5 times their initial size, with volumes that can be a hundred times the initial, injected volume $\langle V_b \rangle$ (fig. 15b, f).

The bubbles eventually burst (fig. 15b, d). On some occasions, bursting reentrains sub-millimetric air bubbles, much smaller than the popped bubble, seen in figure 15b. Bursting also generate droplets, that may travel high and fall back, bounce onto the liquid surface and merge with the bath (fig. 15c). Those drops, especially when they are close to the surface, are difficult to distinguish from the bubbles (fig. 15a, c). As for the large remainder of the surfacing bubbles that do not reach the region of interest, they either move away from it, surfacing the outer side of the rim, or burst before attaining it.

4.2. Raft regime in presence of surfactant

Figure 8b introduced a dense regime of surface bubbles, featuring a higher concentration of surfactant c (when compared to the case in figure 8a), non-coalescing bubbles and the formation of surface bubbles rafts, or clusters. The clusters in figure 8b (or later in figure 17a) are made of almost single-sized bubbles, with diameter $\langle d_b \rangle$. At that particular time, the main cluster covers about one half of the region of interest, being rejoined by smaller clusters and individual bubbles moving around at the surface.

Figure 16 details 30 seconds of typical dynamic activity of the bubbles at the surface in this dense regime, by means of the bubble velocity distributions over time. Horizontal cartesian components v_x and v_y are shown in figure 16a, b, and the velocity norm $v = (v_x^2 + v_y^2)^{1/2}$ is plotted in figure 16c along with the bubbles density ρ_s . Successive phases in the bubbles behavior at the surface can be distinguished. Bubbles sometimes move all as one, having all the same velocity, as is seen at times $t = 0 - 3 \text{ s}$ and $t = 12 - 15 \text{ s}$ in figure 16. Interestingly, this corresponds to a maximal density regime, the surface being entirely covered by bubbles arranged in a hexagonal bidimensional packing: the surface bubbles density is then $\rho_s = \rho_{hex} = 1/2\sqrt{3}\langle d_b \rangle^2$, the density of perfectly aligned disks with constant diameter $\langle d_b \rangle$. Between such coordinated phases, bubbles burst and reaccumulate at the surface and the density ρ_s fluctuates on time scales of order 1 to 5 s (fig. 16c). The velocity distribution is then much broader, indicative of less coordinated motion of the bubbles at the surface.

Figure 17a presents a typical cluster excerpted from the series in the previous figure 16, and zooms in to identify events occurring on individual bubbles at faster time scales (10 to 100 ms, fig. 17b-d). The sequences in figure 17b and c point to events similar to ones already observed in the dilute regime, though happening at a much lower rate: figure 17b shows the coalescence of two bubbles, and figure 17c the bursting of a bubble. Both events leave a blank in the raft, which quickly reorganizes to resorb it. Figure 17d underlines the possibility of a three dimensional organization of the bubbles at the surface: a bubble is initially trapped underneath the raft. However, it quickly emerges and makes its way among its neighbors, in the bi-dimensional cluster. The reverse mechanism, *i.e.* the active trapping of bubbles by the cluster, from 2D to 3D, has not been observed: all trapped bubbles are caught underneath the raft while they try to emerge at the end of their rising, and then they drift away with the raft, staying below it until they ultimately surface amongst it.

The previously described mechanisms: large-scale drifting, bubbles bursting and merg-

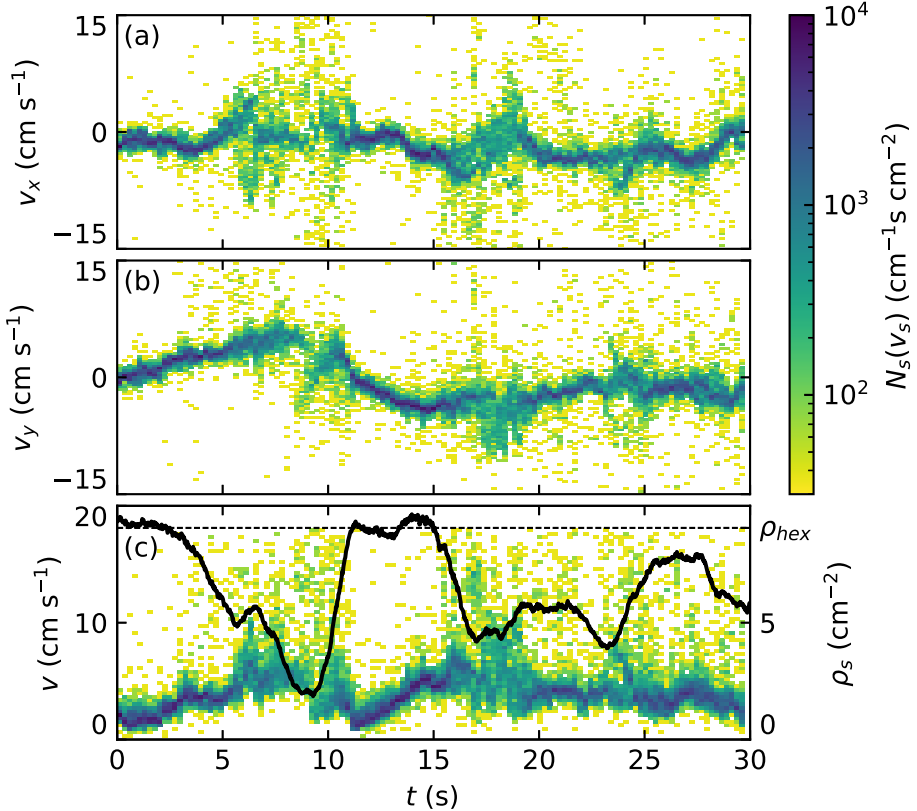


Figure 16: Surface bubble horizontal velocity distributions $n_s(v_s)$ as a function of time, illustrative of the raft regime with surfactants ($c = 92 \mu\text{M}$), at intermediate flow rate $q_v = 63 \text{ cm}^3 \text{ min}^{-1}$ (size in the bulk $\langle d_b \rangle = 3.6 \pm 0.4 \text{ mm}$). (a) v_x and (b) v_y cartesian components, and (c) norm $v = (v_x^2 + v_y^2)^{1/2}$, of the velocity. The concentration of velocities in narrow ranges (dark blue ridges, *e.g.* $t = 0 - 3, 12 - 15 \text{ s}$) indicate a coordinated motion of all bubbles, alternating with less coordinated phases (broader histogram at given times, *e.g.* $t = 8 - 10 \text{ s}, 17 - 19 \text{ s}$). (c, right axis) Surface bubbles density ρ_s . We indicate $\rho_{hex} = 1/2\sqrt{3}\langle d_b \rangle^2$ the density of a 2D hexagonal packing of disks with uniform diameter $\langle d_b \rangle$ (dashed line).

ing, and occasional bubbles trapping, are the ways the ensemble of bubbles spontaneously responds to the steady influx of non-coalescing and long-lasting bubbles. With the exception of the trapped bubbles, and despite high concentrations of SDS, under the experimental conditions presented in this paper no formation of a 3D foam, one natural way to overcome the constant injection of bubbles in a bounded plane, was observed.

5. Surface bubbles statistics

We now turn to a statistical description of the different regimes, over much longer time scales, having shown in figure 8 that the set-up is statistically stationary.

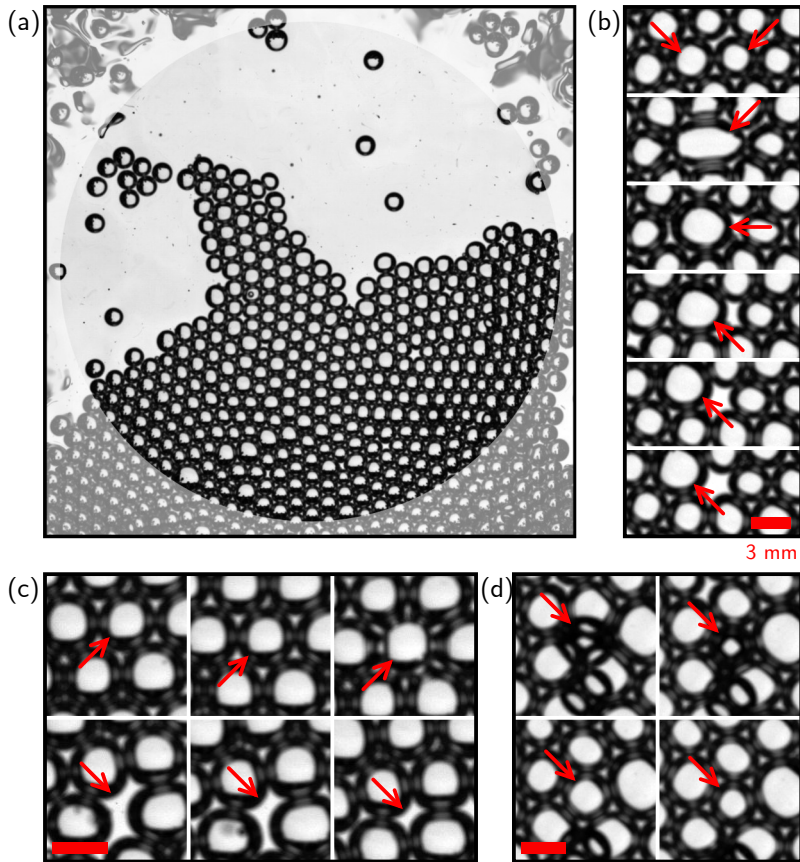


Figure 17: (a) A surface bubbles raft in the presence of surfactant, at intermediate flow rate ($c = 92 \mu\text{M}$, $q_v = 63 \text{ cm}^3 \text{ min}^{-1}$). (b – d) 3 typical events, each reading from left to right, then top to bottom. Consecutive frames are separated by $\Delta t = 24 \text{ ms}$, scale bars are 3 mm wide. (b) Coalescence of two bubbles (second frame). (c) A bubble bursts (third frame), leaving a blank in the raft, which eventually resorbs. (d) A bubble, initially trapped underneath the bubbles raft, surfaces into the raft.

5.1. The case with clean water

When the water is clean, the coalescence of neighbouring bubbles is inevitable (Oolman & Blanch 1986): bubbles at the surface therefore grow in size (figure 15b, d, f), preserving their total volume, until they pop. Figure 18 shows the surface bubble probability distribution function in terms of their volume $V_s(d_s)$ (fig. 18b), as well as the corresponding distributions $n_s(d_s)$ for the sizes measured at the surface and $n_b(d_b)$ in the bulk (fig. 18a). Distributions n_s are given per unit area, so that $\rho_s = \int n_s(d_s) dd_s$, the surface bubbles density. The gaussian distribution in the bulk, centered around the mean size $\langle d_b \rangle$ in the bulk is also shown and matches the first peak of the surface size distribution (figure 18a), confirming that most of the bubbles have indeed the size of the injected bubbles.

Surface bubble volumes V_s are normalized by the volume of the mean injected bubble $\langle V_b \rangle = \pi \langle d_b^3 \rangle / 6$, with the first peak in the surface bubble volumes at $V_s = \langle V_b \rangle$ (figure 18b). The next peaks are located at $V_s / \langle V_b \rangle = 2, 3, 4, 5$, etc, and are the signature of the additivity of volumes during bubbles merging events. The distribution of sizes and

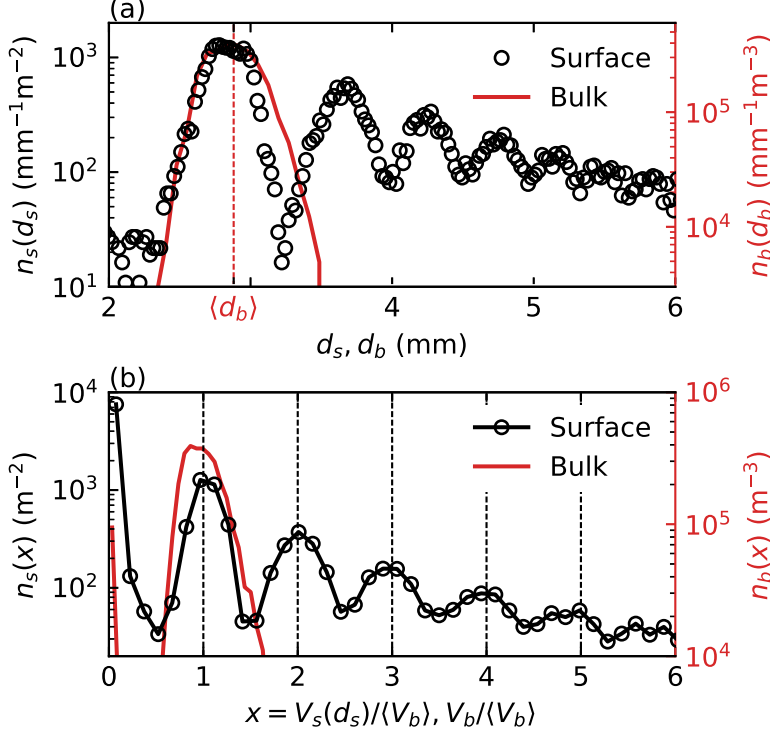


Figure 18: Distributions, for clean water, of bubbles at the surface n_s (left axis, black symbols) and in the bulk n_b (right axis, red), for a low flow rate $q_v = 25 \text{ cm}^3 \text{ min}^{-1}$. (a) Size distributions $n_s(d_s)$ and $n_b(d_b)$. The vertical dotted line indicates the bulk bubble mean size $\langle d_b \rangle$. (b) Volume distributions $n_s(V_s(d_s)/\langle V_b \rangle)$ and $n_b(V_b/\langle V_b \rangle)$, where volumes are normalized by the bulk bubble volume $\langle V_b \rangle = \pi \langle d_b^3 \rangle / 6$. Vertical dotted lines are located at integer values of $\langle V_b \rangle$ and highlight corresponding peaks in the distribution $n_s(V_s/\langle V_b \rangle)$.

volume is therefore extremely broad. This volume conservation, in addition to the air mass conservation at bubbles merging, is a manifestation of air incompressibility under the experimental conditions. Pressure inside the bubbles is $p_{atm} + 4\gamma/R_{cap}$, with p_{atm} the atmospheric pressure, typically 10^5 Pa , γ the air-water interfacial tension and R_{cap} the bubble cap radius. For millimetric bubbles in clean water, the Laplace contribution $4\gamma/R_{cap} \sim 100 \text{ Pa}$ lies well below the atmospheric contribution, and the pressure drop due to the increase in R_{cap} after bubbles merging is negligible, hence the apparent volume conservation.

5.2. Surface size distribution in presence of surfactants

The addition of surface-active material modifies the behavior of bubbles in different ways, preventing bubbles coalescence and increasing their lifetime. Figure 19 shows surface bubble size distributions $n_s(d_s)$ for various concentrations of surfactant SDS, and two different flow rates ($q_v = 31$ and $50 \text{ cm}^3 \text{ min}^{-1}$). Along with the different distributions in figure 19a and b, we present on the side eight snapshots corresponding to each case, to help visualize the gradual changes at the surface.

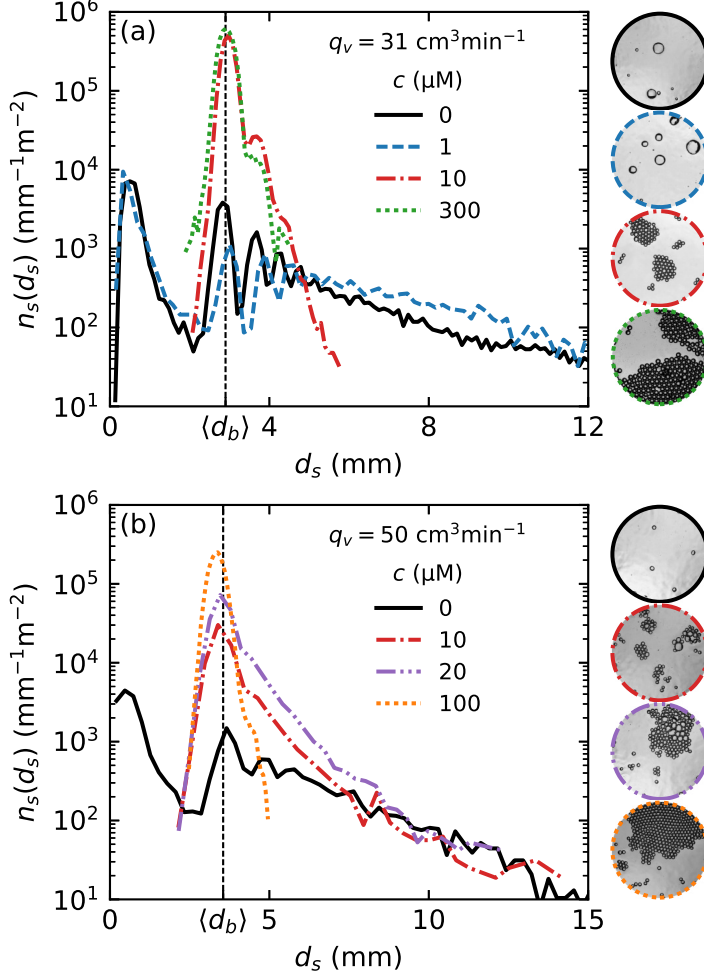


Figure 19: Bubbles size d_s distributions for different SDS concentrations c , below and above the coalescence threshold $c_0 \sim 10 \text{ } \mu\text{M}$, and two flow rates: (a) $q_v = 31 \text{ cm}^3\text{min}^{-1}$, and (b) $q_v = 50 \text{ cm}^3\text{min}^{-1}$. Increasing c above c_0 prevents coalescence and stabilizes bubbles, decreasing the size dispersion, and increasing the density around the bulk size $\langle d_b \rangle$, indicated in the vertical black dashed line. The column on the right shows still images from the respective series.

For clean water and small values of concentration ($c \leq 1 \text{ } \mu\text{M}$), the surface bubble size distribution presents peaks around the mean injection size $\langle d_b \rangle$ and slightly above (fig. 19a and b, solid and dashed lines). This is the signature of the volume-conservative coalescence described in section 5.1. After a few numbers, the successive peaks overlap and contribute to a long, heavy tail, indicating that bubbles still coalesce, at all sizes. We resolve the statistics for bubbles with up to 5 times their injection diameter $\langle d_b \rangle$, which corresponds to a hundred times their injection volume $\langle V_b \rangle$. Although the heavy tail on the diameter distribution exhibits a reasonable agreement with an exponential distribution, we discuss in section 5 that the *volume* distribution is better interpreted by a power-law tail. We rationalize and discuss the argument in section 6.

For a high concentration value ($c \geq 100 \mu\text{M}$), the distribution of d_s is sharply peaked around the peak of injection size $\langle d_b \rangle$ (fig. 19a, b, dotted lines). The surface distribution $n_s(d_s)$ is thus similar to the bulk distribution of sizes $n_b(d_b)$, since coalescence events are suppressed by surface-active contaminants.

An intermediate regime is distinguished for concentrations around $c = 10 \mu\text{M}$. With a low flow rate $q_v = 30 \text{ cm}^3 \text{ min}^{-1}$, a second and a third peaks at approximately $2^{1/3}\langle d_b \rangle$ and $3^{1/3}\langle d_b \rangle$ are still visible and indicate that surfacing bubbles keep merging (fig. 19a, dash-dotted line). However, they do so in much smaller proportions, 10 to 100 times less, when compared to the value of the distribution $N_d(d_s)$ around the injection size $\langle d_b \rangle$. At the higher flow rate $q_v = 51 \text{ cm}^3 \text{ min}^{-1}$, the transition from a heavy-tailed distribution (coalescence regime) to the peaked distribution around the injection size $\langle d_b \rangle$ (non-coalescence regime) is more gradual (fig. 19b, dash-dotted lines). In this case, bubbles still coalesce to populate larger sizes, in proportions similar to the case without surfactant. But even more bubbles stay around the injection size $\langle d_b \rangle$, hence narrowing the distribution around the major peak.

We acknowledge the production of bubbles with sizes much smaller than $\langle d_b \rangle$. Figures 19a and b show a large number of events around $d_s = 500 \mu\text{m}$, in the cases with $c \leq 1 \mu\text{M}$ (solid and dashed lines. Those small bubbles are not detected in the cases with a higher c , due to a difference in the bubbles detection algorithm, but may be seen on the third- and second-to last snapshots in figure 19). This peak aggregates indistinguishably: sub-millimetric bubbles surfacing from the bulk (see section 2.3.2), bubbles being formed at the collapse of a bursting bubble cavity, air pockets trapped under the retracting and collapsing bubble cap when bursting, as well as droplets falling back on the water surface after being ejected during a bubble bursting event.

Eventually, figure 19 highlights an extremely important result from a practical point of view: in case of relatively clean water, where bubbles coalescence is possible, the *surface* size distribution is much broader than the *bulk* size distribution of bubbles, so that *surface* bubble distributions should be considered when thinking of sea spray production.

5.3. Bubbles surface fraction and clustering

Figures 8c and e already disclosed the major trend discussed in this article, that the bubbles surface density ρ_s increases with an increased surfactant concentration c . Figure 19 then outlined that increasing c also led to a sharp decrease of the bubble variability around the mean injection size $\langle d_b \rangle$. However, $\rho_s = \int n_s(d_s) dd_s$, the 0-th moment of the size distribution, does not incorporate any bubble size information, and we need to turn to its second moment:

$$\phi_s = \frac{\pi}{4} \int_{d_s} n_s(d_s) d_s^2 dd_s. \quad (5.1)$$

In the current representation, ϕ_s is non-dimensional and, physically, is the surface area covered by the bubbles or *bubbles surface fraction*.

Figure 20 shows the evolution of the bubbles surface fraction ϕ_s as a function of the experimental control parameters for both surfactants SDS and Triton X-100: air flow rate q_v (fig. 20a, b) and surfactant concentration c (fig. 20c, d). Figure 20a, b highlights the general increase of ϕ_s with the flow rate q_v , with color encoding the surfactant concentration c . The trend is particularly clear with clean deionized water (empty symbols), where an increase in the flow rate q_v from 20 to 120 $\text{cm}^3 \text{ min}^{-1}$ leads to a factor 10 gained in the bubbles surface fraction ϕ_s , from 10^{-2} to 10^{-1} . For equivalent flow rates, a smaller needle size leads to higher values of ϕ_s (fig. 20a, symbol size), which is mediated by the higher number of bulk bubbles of small size generated at the needles

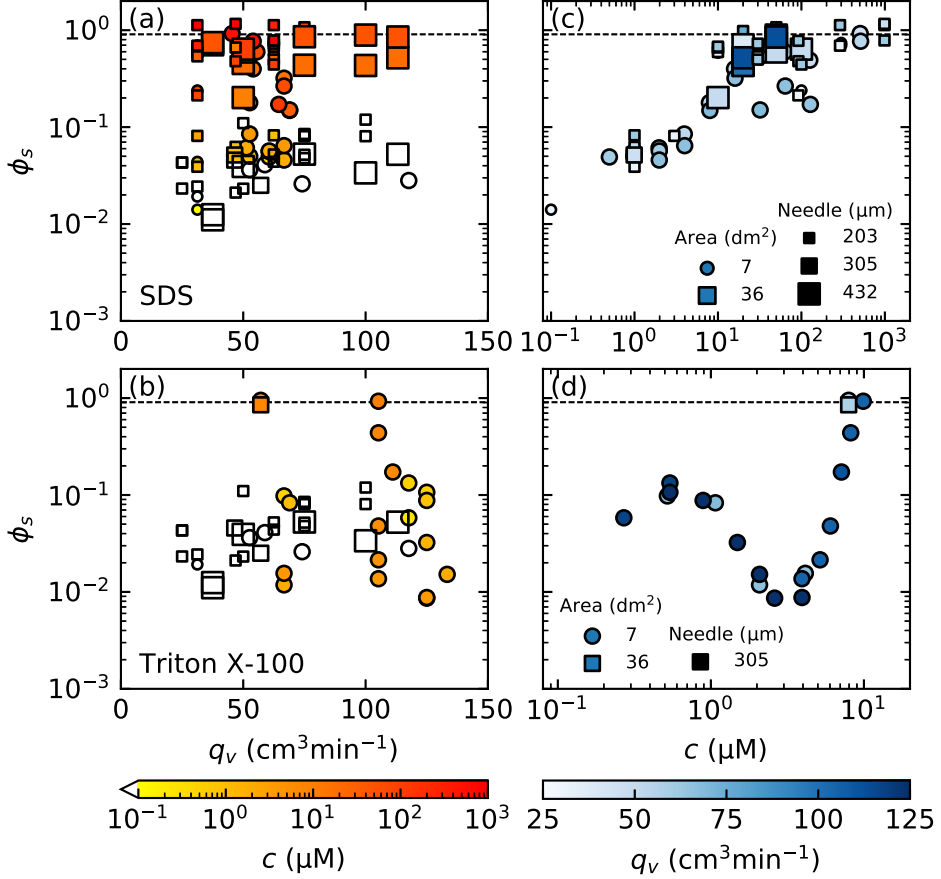


Figure 20: Bubble surface fraction ϕ_s as a function of: (a, b, or left) the air flow rate per needle q_v ; and (c, d, or right) the surfactant concentration c , for surfactants (a, c, or top) SDS and (b, d, or bottom) Triton X-100. Cases with deionized water are shown in empty symbols. The horizontal dashed black line at $\phi_{hex} = \pi/2\sqrt{3}$ is the bidimensional hexagonal arrangement of monodisperse hard disks. A variety of bubbling conditions are indicated in the different symbols: their sizes stand for different needle inner diameters (203 to 432 μm), squares and circles for different surface areas available to bubbles (full tank: 36 dm^2 and restricted area: 7 dm^2 , respectively).

tip, as was shown in figure 6. With SDS, when increasing the surfactant concentration from 0.1 μM (fig. 20a, yellow symbols) to 1 mM (red symbols), ϕ_s increases and quickly reaches the value $\phi_{hex} = \pi/2\sqrt{3}$. This upper bound is barely overcome, as it is the maximal value for ϕ_s , for a perfectly hexagonal arrangement of monodisperse particles. Note that values higher than ϕ_{hex} in figure 20 are either an effect of compression of the bubbles assembled in rafts at the surface, or simply an experimental error (the raft dense detection method, as described in appendix A, might lead to some slight, non-physical, overlap of bubbles on the plane (see for example figure 8b)). This potential error remains in the global level of dispersion of our experimental data.

Figure 20c, d presents the same data for the bubbles surface fraction ϕ_s , now as a function of the surfactant concentration c (fig. 20c for SDS, fig. 20d for Triton X-

100), with the color encoding the air flow rate. The two regimes identified above are retrieved, for both surfactants. At low levels of surfactant concentration, bubbles burst and coalesce quickly and bubbles have a small imprint on the surface: ϕ_s is low. Above a certain concentration (20 μM for SDS, 10 μM for Triton X-100), the surface becomes saturated with single-sized, long-living bubbles and the upper limit $\phi_s = \phi_{hex}$ is reached. For even higher surfactant concentrations, bubbles will pile up in multiple layers, making any reliable measurements impossible in the present configuration.

Interestingly, the transition between the two regimes is continuous, even though it occurs on a limited range of concentration. It is especially visible from figure 20c (SDS) that the details of the bubble production (air flow rate, needle size, needles number, total surface area available to bubbles), have, in the explored range of parameters, a limited impact on the transition from clean to contaminated regimes. The precise behavior of the bubbles in the transition from clean to contaminated regimes may finally depend on a variety of parameters. The surfactant itself, as seen when comparing figures 20c and d, seems to have a primary role. The global trend for SDS, though blurred by variabilities in other parameters, is a smooth increase over two orders of magnitude. Conversely, Triton X-100 undergoes a non-monotonous transition, increasing from the clean regime to concentrations around $c \approx 0.6 \mu\text{M}$, then decreasing up to $c \approx 3 \mu\text{M}$, before rising again sharply to $\phi = \phi_{hex}$ at $c \approx 10 \mu\text{M}$. Among other parameters of a lesser importance, the total area available to bubbles may influence the way bubbles emerge at the surface, and thus modify α in ways that may contribute to the scatter of data (fig. 20c).

This non-trivial transition reaffirms the need for an accurate description of bubbles behavior at the surface, that we understand as a surface transfer function. As a last remark, we emphasize again that these variations all occur for low values of surfactants, when compared to the critical micellar concentration (respectively 8.2 mM and 220 μM for SDS and Triton X-100).

5.4. Order at the surface

The radial distribution function is another way of quantifying the level of order in the bi-dimensional assembly of bubbles, and is exhibited in figure 21 for different concentrations of surfactant. It states, for a bubble individualized in the set, the likelihood of finding a neighbor at a distance χ_s from its center. A value of 1 at all distances means that there is no preferential separation distance, which is the case for the clean water — regardless of the meniscus interactions, which do not set any equilibrium distance. For high values of c , the structure of the hexagonal close packing appears, with well-defined peaks at distances $\chi_s/\langle d_b \rangle = 1, \sqrt{3}, 2, \sqrt{7}, 3$, etc. The experimental illustration by Bragg & Nye (1947), exhibited here as a reference, was making the case of the atomic crystalline structure with a bi-dimensional “perfect crystalline raft of bubbles”.

6. A model for collective surface bubble statistics

We now develop a phenomenological model, with analytical foundations and a computational implementation. We aim at reproducing and rationalizing the surface statistics described in section 5 with minimal physical ingredients. The steps included in the model formulation are rooted in the physical observations made in the sections 3, 4 and 5, which we recall here:

- bubbles are introduced at the surface at a constant rate;
- bubbles are introduced with a unique size;
- depending on the surface contamination, bubbles can either grow in size by coalescence, or cluster in rafts;

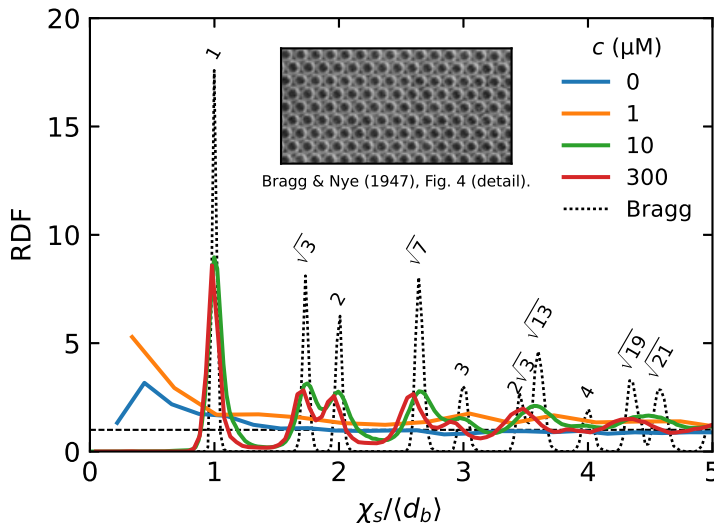


Figure 21: Radial function distribution for an increasing concentration of SDS, below and above the threshold for coalescence $c \approx 6 \mu\text{M}$ (solid lines). The dotted black line is computed from Bragg & Nye (1947), fig. 4, which illustrates a “perfect crystalline raft of bubbles” with diameter $\langle d_b \rangle = 0.3 \text{ mm}$. The numbers are the exact locations of neighbors in a hexagonal close packing of hard disks with diameter 1.

- coalescence events preserve the total volume of the bubbles involved;
- bubbles have a finite lifetime and finally disappear by bursting.

The model formulation and its numerical implementation are described in §6.1. The outcomes of the cellular automaton are then compared with experimental data in §6.2, in both clean and contaminated regimes. We also discuss the role of the numerical parameters, and how they identify to their experimental counterparts. The scope of the model is finally discussed in §6.3

6.1. Discrete model and cellular automaton implementation

A discrete model is developed that features the physical arguments enumerated above. We consider an ensemble of bubbles with discrete diameters d_k ($k \geq 1$), scattered on a plane with surface area \mathcal{A} . Bubbles with size d_k have a density n_k (*i.e.* number of bubbles with size d_k , divided by \mathcal{A}), evolving according to the three mechanisms identified previously: bubble production, coalescence, and bursting. Bubble merging, in particular, is the only way (under a production of monodisperse bubbles) for bubbles to grow in size and populate higher ranks $k > 1$. When they coalesce, bubbles i preserve their total volume $\sum_i d_i^3$, so that the ensemble contains only bubbles with sizes $d_k = k^{1/3} d_1$.

In this representation the first moments of the distribution of sizes $n_k(d_k)$ yield important physical content. The moment of order 0 is the bubbles surface density:

$$\rho_s = \sum_{k \geq 1} n_k, \quad (6.1)$$

the first moment is the mean bubble size:

$$\langle d_s \rangle = \frac{1}{\rho_s} \sum_{k \geq 1} n_k d_k, \quad (6.2)$$

and the second moment is directly proportional to the bubbles surface fraction ϕ_s :

$$\langle d_s^2 \rangle = \frac{1}{\rho_s} \sum_{k \geq 1} n_k d_k^2 = \frac{4}{\pi} \frac{\phi_s}{\rho_s}. \quad (6.3)$$

Note eventually that the motion of bubbles, specifically their mutual attraction *via* meniscii interactions, are not modelled here, as we are interested in much longer, integrated and statistically independent time scales.

6.1.1. Numerical implementation

The numerical implementation of the model is a cellular automaton. The ensemble of bubbles (sizes d_k , densities n_k) undergoes, at each iteration in the simulation, the following steps, where we define the parameters of the simulation.

(i) New bubbles with size d_1 are introduced in the set with production rate p_1 , per unit area (per iteration). This rate is chosen to be a random variable normally distributed, with a dispersion of typically $\pm 20\%$ around its mean.

(ii) Bubbles are removed from the set according to their age s (*i.e.* time spent in the simulation): old bubbles are more likely to burst than young ones. The bubble lifetime distribution is modelled by a Weibull distribution with shape parameter $4/3$, following equation (3.9) in Lhuissier & Villiermaux (2012). The cumulative distribution function, evaluated at bubble age s , is naturally the bursting probability for each bubble, at each simulation step. The distribution is scaled by τ , the mean bubble lifetime, given in simulation steps.

(iii) The bubbles of the set are scattered randomly, with a uniform spatial distribution, over the total available surface area \mathcal{A} .

(iv) Bubble pairs whose edge-to-edge distance lies under a certain criterion ℓ may merge into a new bubble, according to a pair-coalescence probability m . If merging, they add up their volumes. Bubble pairs are considered by increasing distances (closest merge first), with no iterative handling of triplets of overlapping bubbles, or more. In the event of overlapping bubbles, and at low enough bubbles surface fraction, potential anomalies are assumed to resorb at the next iteration, when bubbles are shuffled again. The age of the merged bubble is set to $s = 0$.

(v) Bubbles are passed on to the next iteration with their age s increased by one iteration $s + 1$.

The merging scheme (iv) is based on the assumption that 2 bubbles at the surface of clean water, when close enough, will attract and finally merge with probability m ($m = 1$ in clean water, and decreases with the surface contamination Oolman & Blanch (1986); Vella & Mahadevan (2005)). Note that the probability m is taken independent of the bubble size. The threshold distance, ℓ in the computational model, is the typical length over which bubbles start or cease to attract each other. Physically, it represents the bubbles meniscus typical size and scales as the capillary length of the liquid ℓ_c . By setting and holding $\ell = d_1$, we set the bubbles unit size d_1 around the capillary size, a situation similar to experiments (see section 2).

Figure 22 illustrates the outcome of a typical simulation in a coalescence regime ($m = 1$), by plotting the bubbles density ρ_s and mean size $\langle d_s \rangle$ as a function of the successive iterations s . The domain size is $\sqrt{\mathcal{A}} = 30 d_1$, with $p_1 \mathcal{A} = 9 \pm 2$ bubbles introduced per iteration, and the bubble mean lifetime is $\tau = 10$ iterations. Figure 22a, c zooms in the first instants of the simulation, run for a variety of initial conditions (1 to 60 bubbles, all with size d_1). As seen in both the surface density ρ_s and bubble mean size $\langle d_s \rangle$, the bubbles system reaches a stationary state within a relatively small number of iterations, typically 10 to 20. Figure 22b, d follows a single simulation on a much larger number of

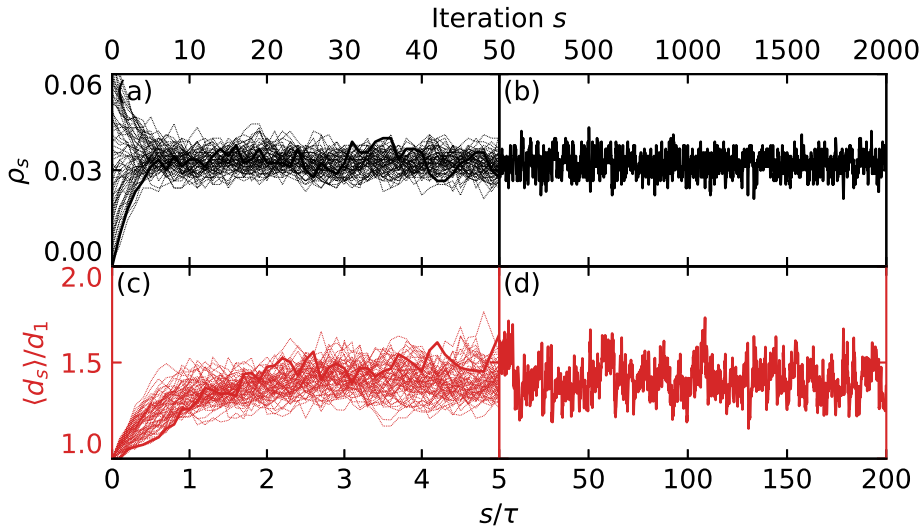


Figure 22: Evolution of (a, b) the bubbles density ρ_s (black lines) and (c, d) mean diameter $\langle d_s \rangle / d_1$ (red lines) in the course of a simulation run. At each iteration, $p_1 \mathcal{A} = 9 \pm 2$ bubbles are introduced on a square with side $\sqrt{\mathcal{A}} = 30 d_1$. Bubble mean lifetime is $\tau = 10$ iterations so that the total run is 200τ . (a, c) Zoom on the first 50 iterations, showing the transient, from different initializations (0 to 60 bubbles with size d_1 , thin lines), to a stationary state. (b, d) View of a single simulation over a larger number of iterations.

iterations (up to 2,000, or 200 bubble mean lifetime), and helps appreciate the system stationarity on the long run. A final comparison of the simulation at short times, with multiple runs (fig. 22a) and of a single run over long times (fig. 22b), makes the case for an equality, in a statistical sense, of ensemble and time averages.

6.2. Role of the model controlling parameters and comparison with experiments

A quantitative comparison of the model with the surface statistics requires to inform the simulation production rate p_1 , pair-coalescence probability m and bubble mean lifetime τ with characteristic scales inferred from experiments, respectively the surface bubbles production rate p_s (§2.3), merging rate q_m and bursting rate q_b (§3), which we are doing in the next paragraphs.

6.2.1. Coalescence regime

The coalescence regime (clean deionized water, see §5.1) is a peculiar case where bubbles systematically merge when close enough, and they burst at a fixed rate. Therefore, the pair-coalescence probability is set to $m = 1$, and the bubble mean lifetime to some value large enough for bubbles not to burst immediately after they are introduced or merging (typically around 10 iterations, at least).

The only parameter left to vary is then the bubble production rate. Experimentally, bubbles are introduced in the bulk at various flow rates q_v , which amount to various bubbling rates p_s into the imaged region (surface area \mathcal{A}). p_s is made non-dimensional by expressing the available area in units of $\langle d_s \rangle$, and time in units of the surface bubble

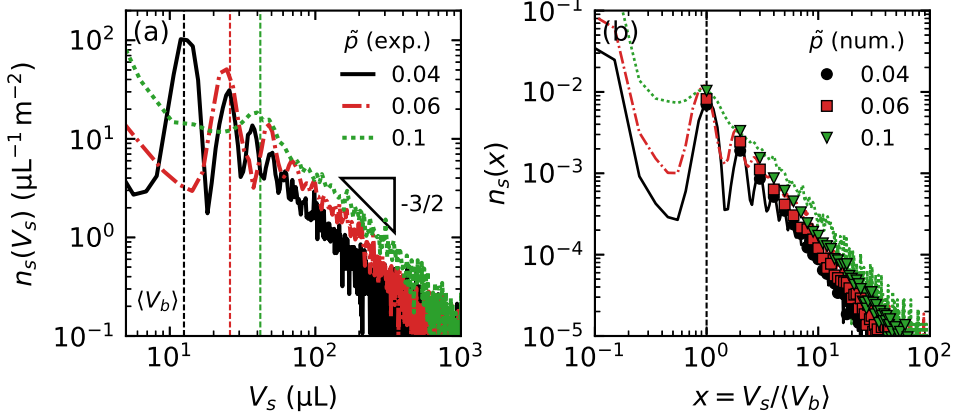


Figure 23: Experimental and simulated surface bubble volume distributions, in the coalescence regime. (a) Experimental distributions (lines), for 3 different flow rates $q_v = 25, 50, 100 \text{ cm}^3 \text{ min}^{-1}$ in clean water (resp. $\tilde{p} = 0.04, 0.06, 0.1$). Vertical dashed lines indicate the average bulk volume $\langle V_b \rangle$ in each case. (b) Lines duplicate the experimental distributions in (a), volumes being normalized by $\langle V_b \rangle$ (x -axis) and counts by the surface area in units of $\langle d_b^2 \rangle$ (y -axis). The markers are for 3 simulated distributions, with respective production rates $\tilde{p} = 0.04, 0.06, 0.1$ and lie on top of the experimental distributions.

mean lifetime $\langle \tau_s \rangle$. By equations (2.2) and (2.3), this is:

$$\tilde{p}(\text{exp.}) = \alpha \frac{\pi \langle d_b \rangle^2}{4\mathcal{A}} p_b \langle \tau_s \rangle = 1.086 \alpha \frac{N_{\text{needles}}}{\mathcal{A}} q_v^{3/5} g^{1/5} \langle \tau_s \rangle. \quad (6.4)$$

We consider in the following a fixed value of $\alpha = 1/3$, thought of as a generic order of magnitude, but acknowledge that its precise value might slightly change with the flow rate or the total area available to bubbles, due to complex raft dynamics which go beyond the scope of a strictly statistical description (bubbles and raft drifting, surface flows, etc.). The mean bubble lifetime is estimated as the one of a single bubble bursting $\langle \tau_s \rangle \approx 1 \text{ s}$ at 20°C (Poulain & Bourouiba 2019). This value is consistent with the bursting rates q_b measured in the bubble raft decay, at low concentrations of surfactant (§3.3). $\tilde{p}(\text{exp.})$ is finally calculated and takes values, in the clean water cases, in the range 0.01–0.1 (*i.e.* 0.01 to 0.1 bubbles introduced in the system per mean lifetime).

The corresponding expression for \tilde{p} in the model is straightforward and reads:

$$\tilde{p}(\text{num.}) = p_1 \tau. \quad (6.5)$$

Figure 23 compares experiments and simulations in the regime of clean water ($m = 1$). Figure 23a shows experimental distributions of bubble volumes at the surface of clean water, under three air flow rates (*i.e.* bubbles production rates), in physical units (lines). The surface densities are relatively low and a long power-law tail emerges from the logarithmically scaled graph: $n_s(V_s) \propto V_s^r$, with an exponent $r \simeq -3/2$. Note that we do not have a theoretical argument for this robust power-law distribution. Also note that for increasing flow rates, the amplitude of the peak at $V_s = \langle V_b \rangle$ decreases, indicating a lower bubbling rate as predicted by equation (2.2).

In figure 23b, experimental bubble volumes are normalized by their respective injected bulk volume $\langle V_b \rangle$, and their numbers by the monitored area now expressed in units

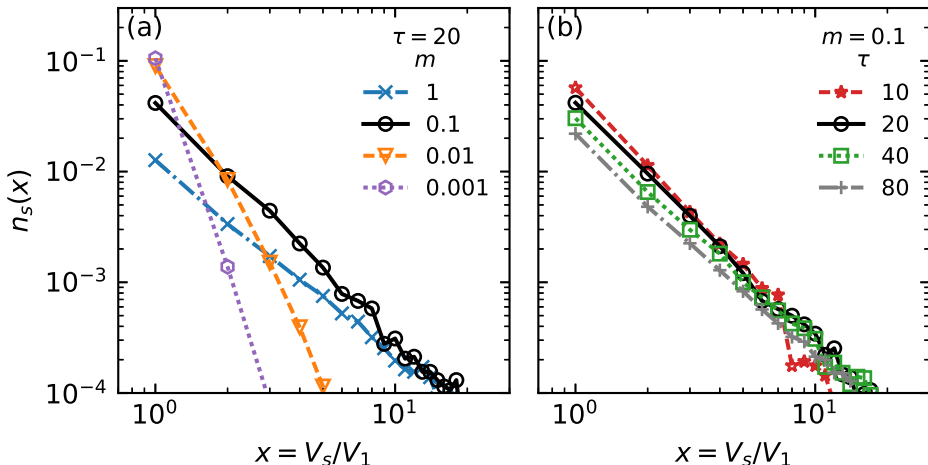


Figure 24: Simulated surface bubble volume distributions, in the partial coalescence regime with a fixed bubble production $\tilde{p} = 0.1$. (a) The pair-coalescence probability is decreased from $m = 1$ to 10^{-3} , with a fixed mean lifetime $\tau = 20$. (b) The mean lifetime is increased from $\tau = 10$ to 80, with a fixed pair-coalescence probability $m = 0.1$.

of $\pi \langle d_b^2 \rangle / 4$, leading to the normalized surface size distribution $n_s(x = V_s / \langle V_b \rangle)$. They are directly compared to three simulated distributions, run for the same values of $\tilde{p} = [0.04, 0.06, 0.1]$ (symbols). Mean lifetime is $\tau = 16$ iterations, domain size $\sqrt{A} = 100 d_1$, and increasing production rate $p_1 = [2.5, 3.7, 6.2] \times 10^{-3}$. We observe strong similarities between the experimental and simulated simulations on both the power-law tail of the distributions, with the same exponent $r = -3/2$, and the evolution of their amplitude, with an increased bubble production at $V_s = \langle V_b \rangle$ (V_k/V_1 in the automaton) leading to more bubbles $n_s(V_s)$ at *all* volumes V_s . Given the assumptions of the automaton model, the agreement is remarkable. The remaining discrepancies are attributed to the uncertainties on α and $\langle \tau_s \rangle$ when computing $\tilde{p}(\text{exp.})$ (eq. (6.4)).

In the coalescence regime, the transfer function from the bulk to the surface transforms narrow, monodisperse bubble distributions into broad, power-law tailed distributions. Our parameterization for this transfer function highlights the role of merging events. It captures successfully, thanks to the identification of the non-dimensional bubbling rate \tilde{p} , the main features of the experimental observations: orders of magnitude, distribution shape and trends.

6.2.2. Merging and bursting in the cellular automaton

As shown in section 3, the addition of surfactants in water has two distinct effects, on the ability of the bubbles to coalesce, and on their individual lifetime. In the automaton simulation, both effects are entirely decoupled: the merging ability is modeled by the individual pair-coalescence probability m , whereas the lifetime is specified by the shape of the lifetime distribution and its scaling τ . Figure 24 shows surface bubble volume distributions from simulations for various merging probabilities m (figure 24a) and mean lifetimes τ (figure 24b), under a fixed bubble production rate $\tilde{p} = 0.1$. In figure 24a, the pair-coalescence probability m is decreased from 1 (the merging of eligible bubbles is systematic) to 10^{-3} , with a fixed mean lifetime $\tau = 32$ iterations. The respective

distributions narrow gradually around the bubble injection volume V_1 , reproducing faithfully the main feature of the transition from clean to contaminated regimes.

In figure 24b, the mean lifetime τ is increased from 16 to 128 iterations, for a fixed pair-coalescence probability $m = 0.1$. The change in τ , at fixed \tilde{p} , has no observable effect on the shape of the distribution. It has, however, a moderate effect on the scaling of the distribution: longer lifetimes τ , because bubbles spend in average more time in the simulation and are therefore more likely to undergo a successful merging event, lead to *fewer bubbles* populating all sizes, *i.e.* a decrease in the overall distribution levels. It is worth recalling here that τ is also involved in the calculation of $\tilde{p} = p_1\tau$ (eq. (6.5)), which is kept constant. An increase in τ while considering a constant bubble production p_1 , instead of a constant \tilde{p} , will result more intuitively in an increase of the overall bubble numbers.

With the two parameters m and τ , the simulations are able to reproduce the phenomenology described in the presence of surfactant in figure 19 in a spectacular way. On the one hand, the distribution shape is controlled by m , from very broad at high value of m to more and more narrow as the merging efficiency is decreased to 0. On the other hand, the lifetime τ plays directly on the amplitude of the distribution, which increases with increasing lifetime.

We now perform a more detailed and quantitative comparison of experiments and simulations, using the dynamical measurements of merging and bursting rates made in section 3 to tune and match m and τ with their physical counterparts.

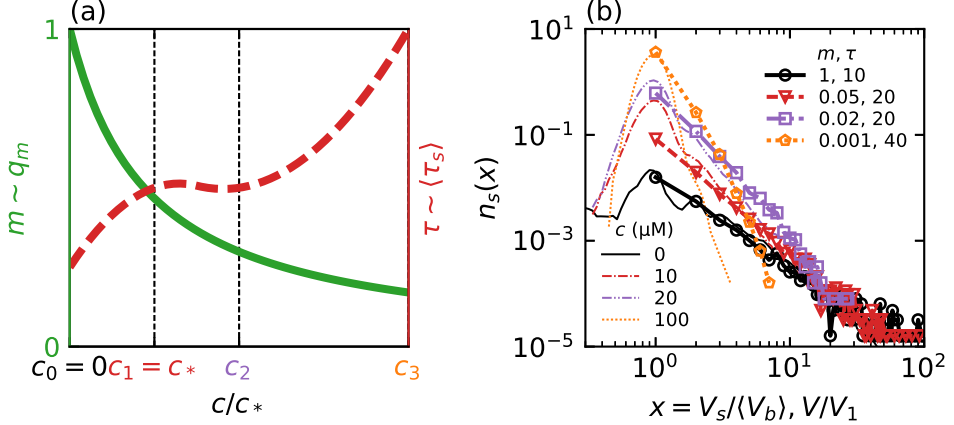
6.2.3. Partial coalescence regime

Experimentally, variations in the partial coalescence regime are achieved by modifying the sole concentration of surfactant c , whereas the numerical model can vary with both the pair-coalescence probability m and the mean lifetime τ independently. Recalling findings from §3, below a transition concentration c_* , coalescence dominates the life of an assembly of bubbles. Merging then depends on the bubbles surface fraction ϕ_s (bubbles attract and merge when they are close enough), and so does bursting. Above c_* , coalescence vanishes quickly with increasing surfactant concentration, in a progression that we consider geometric for simplicity, and similar for both the merging rate q_m and pair-coalescence probability m : $m \sim q_m \sim c^{-\beta}$, with $\beta = 1.5$.

The evolution for the bubble mean lifetime $\langle\tau_s\rangle$ is less critically dependent on the coalescence transition, as $\langle\tau_s\rangle$ globally increases with the concentration of surfactant (Lhuissier & Villermaux 2012; Modini *et al.* 2013; Champougny *et al.* 2016). When coalescence becomes negligible, *i.e.* for high surfactant concentrations $c \gg c_*$, $\langle\tau_s\rangle$ is well approximated by the global decay time τ_r of the raft, as measured in section 3 (fig. 11): $\tau_r \approx 1/q_b \sim \langle\tau_s\rangle$. In particular, the global raft decay time τ_r was observed to plateau across the transition, before increasing again. We represent schematically these trends for the merging rate q_m and bubble mean lifetime $\langle\tau_s\rangle$ in figure 25a, as a basis for the choices of parameters.

A case-by-case comparison between experimental and simulated bubble distributions is plotted in figure 25b, from a clean water case ($c_0 = 0$), across the coalescence transition ($c_1 \approx c_*$ and $c_2 = 2c_1$) and asymptotically further into the partial to no-coalescence regime ($c_3 = 10c_1 \gg c_*$). The experimental values and trends for the bubble merging rate q_m and lifetime $\langle\tau_s\rangle$, though not exactly matching the definition of their numerical counterparts, inform the choice of parameters m and τ in the following way.

- The first case is taken in clean water $c_0 = 0$ μM : $m_0 = 1$, as discussed in section 6.2.1. It helps us match the production rate $\tilde{p}_0 = 0.1$, and the initial bubble lifetime $\tau_0 = 10$ iterations.



(c) Numerical parameters

c/c_*	τ (iter.)	m	\tilde{p}
0	10	1	0.1
1	20	0.05	0.2
2	20	0.02	0.2
10	40	0.001	0.4

Figure 25: Comparison of experimental and simulated surface bubble distributions, in the partial coalescence regime. (a) Schematic trends for merging rate q_m (green solid line), bubble lifetime $\langle \tau_s \rangle$ (red dashed line, see also §3), associated with numerical parameters m and τ , respectively. 4 concentrations of surfactant are selected below ($c_0 = 0$), around ($c_1 \simeq c_*$, $c_2 = 2c_1$) and above the transition ($c_3 = 10c_1 \gg c_*$), to compare to numerics. (b) Bubble volume distributions, in the statistically stationary experiment for increasing concentrations c of SDS (thin lines, reproduced from figure 19 in a non-dimensional way), and from the cellular automaton (thick lines and symbols). Simulations are run with a constant bubble production $p_1 = 0.01 \pm 25\%$ on a domain with size $\sqrt{A} = 40 d_1$. Numerical curves are shifted vertically for clarity. The variations and selection of m and τ follow the trends in (a). Their values are summarized in the table (c), and discussed in the text.

- Next, the surfactant concentration (SDS) is increased to $c_1 = 10 \mu\text{M}$, *i.e.* around the transition concentration c_* . The merging probability is decreased to $m_1 = 0.05$, and the mean lifetime is increased to $\tau_1 = 20$ iterations, matching the sharp reduction in the bubbles merging ability and the increase in bubble lifetime.
- In the third case, the SDS concentration is increased further $c_2 = 20 \mu\text{M}$, above the transition and into the plateau of the raft decay time. $\tau_2 = 20$ is thus kept constant. The coalescence probability is decreased according to the geometrical decay $m_2 = m_1(c_1/c_2)^\beta \approx 0.02$.
- In the last case, $c_3 = 10c_1 = 100 \mu\text{M}$, and thus $m_3 = m_1/10^\beta \approx 0.001$. Having reached the end of the plateau, the bubble mean lifetime is increased further to $\tau_3 = 40$ iterations.

As seen in figure 25b, and given the somewhat coarse approach, the agreement is good. The shapes of the numerical distributions, with the parameters m and τ varied according to an inferred evolution with respect to a unique surface contamination control parameter

(the surfactant concentration c in the experiments), narrow down gradually around the injection volume V_1 , in a similar way as in the experiments. As a last remark, we do not fully capture the strong increase in the amplitude of the experimental distributions, as c is increased. This is attributed to the fact that bubbles can overcome the meniscus length and stay in close contact in the experiment (see for example figure 8b), which does not happen in the simulation without modifying the numerical meniscus distance ℓ .

6.3. Discussion of the transfer function from bulk to surface controlling parameters

We demonstrate with figures 23, 24 and 25 that the parameterization of the bubbles transfer function from the bulk to the surface depends on a limited number of variables, which we identify. Bubbles merging —when coalescence is likely to happen— is essential to build broad distributions from monodisperse bubbles, and depends directly on the pair-coalescence probability m . Preventing coalescence (*i.e.* decreasing m) therefore narrows the surface distribution around the bubbles bulk size, but fails to explain the large increase in absolute number of bubbles at the surface, as observed experimentally. This increase is first attributed to the bubbles production rate, which has a direct influence on the surface density, as was shown in figure 23b.

However, when the production rate p_1 is kept constant, the bubble mean lifetime τ is the second parameter that influences the bubbles density. We recall that τ scales the global bubbles lifetime distribution, where old bubbles are more likely to burst than young ones. With an increased mean bubble lifetime τ , and the number of bubbles being introduced at each iteration being the same, bubbles thus last longer before bursting, in average, which *de facto* increases the population at the surface. Experimentally, an increased concentration of surfactant modifies the two parameters τ and m , where the numerical model allows their independent study.

Conversely, and as a final comment, a small mean lifetime will not only interfere with the bubbles production, but also with the coalescence “dynamics”, which has no intrinsic time scale other than the simulation step s . A drastically small τ would thus burst bubbles before they are even able to merge, keeping the surface bubbles distribution narrow around the injected size, and to low density value.

7. Conclusion

This article demonstrates that, in the overall process of spray production by bursting bubbles, coming for instance from breaking wave events, knowledge of the *bulk* bubbles distribution is not enough to predict the *surface* bubbles distribution, and hence shall certainly fail to predict alone the spray properties accurately (number, sizes). We rejoin a cohort of authors in claiming that surface contamination controls the behavior of the bubbles at the surface (Garrett 1967; Prather *et al.* 2013; Modini *et al.* 2013), and draw a precise experimental picture of its role on large assembly, or clusters, rafts or even whitecaps, of bubbles. With no doubt, the minute description of this intermediate stage between bulk bubbles production and spray formation, the *bulk-surface transfer function*, will prove useful in the finer characterization of the spray drops themselves, and identification of the (collective) mechanisms at play.

Depending on the surface contamination, presently modelled by surfactants sodium dodecyl sulfate and Triton X-100, a nearly monodisperse assembly of millimetric air bubbles produced identically in the bulk of a water bath behave in very different ways at the surface. Two asymptotic regimes are identified by means of experiments measuring the dynamics and the statistics of such assemblies, and confirmed by a cellular automaton model based on a handful of physical arguments. Their distinctive features are:

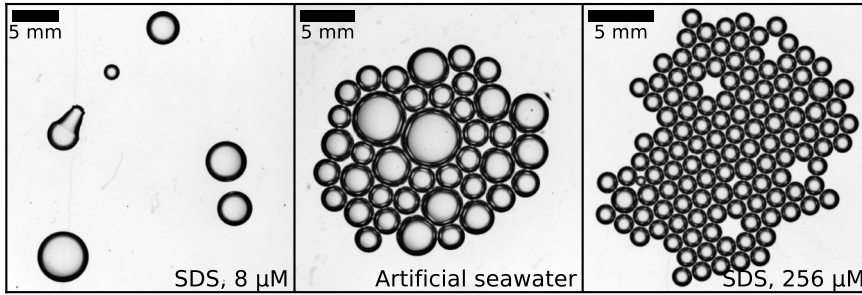


Figure 26: Three snapshots of rafts in, from left to right, deionized water and SDS ($c = 8 \mu\text{M}$), artificial seawater, and deionized water and SDS ($c = 256 \mu\text{M}$), under similar room conditions and bubble production. They illustrate where seawater stands with respect to merging and bursting: in a partial coalescence regime, between the asymptotic clean and fully contaminated regimes.

- a clean surface regime, with short-lived and coalescing bubbles, exhibiting low surface density and fraction, despite large bubbles resulting from the merging of up to a hundred bubbles of the initial size.
- a contaminated surface regime, with long lasting and non-coalescing bubbles, where the surface bubbles distribution tends towards the bulk bubbles distribution for high levels of contamination, and surface density, surface fraction and order tend towards a hexagonal network of bubbles, the arrangement which maximizes packing in two dimensions.

The transition between these two regimes appears to depend on the surfactant itself, in a non monotonous, non trivial fashion. The identification and use of the global merging and bursting rates q_m and q_b is a first step towards the parameterization of the bulk-surface transfer function, envisioned here from a dynamical point of view. It temporarily allows to go around the need for a chemico-physical analysis of the water interface, as could be the case when performing the experiment with liquids of partially known composition (*e.g.* seawater scooped out of the open ocean). However, a precise link to the physico-chemistry of the interface will be required in the pursued ambition of a complete parameterization of the bulk-surface transfer function.

The case with seawater, with a more complex chemical and biological composition, is certainly lying between those regimes. Figure 26 shows a visual comparison of three rafts of bubbles, produced under similar laboratory conditions, respectively in the clean regime, with artificial seawater and in the contaminated regime. In seawater, the presence of bubbles with multiple sizes is a clear indication that bubbles merge *and* burst at the same time: it is a last demonstration of the need for a comprehensive bulk-surface transfer function.

The discrete formulation we derive for bidimensional assemblies of bubbles gives physical grounds to a numerical and statistical implementation of the bulk-surface transfer function. It takes the form of a cellular automaton, which is informed by dynamical quantities directly inferred from experiments. Despite the simplicity of the numerical model, distributions shapes, orders of magnitude and trends with respect to the surface contamination and bubbles production rates are retrieved and compared successfully with the experiments. The identification and matching of numerical and experimental parameters is successful, supporting the need for the development of a

more general framework, embracing all contaminations. And eventually linking the bulk bubbles production mechanisms to the spray production in rafts regimes.

In future studies, the statistically stationary bubble plume set-up will offer possible variations on a greater number of parameters, allowing in particular to refine the link with the water physico-chemistry: the needle size(s), down to 200 μm in diameter; the needles number, virtually any number between 1 and 48. the water temperature, from room temperature to multiple tens of degrees celsius; its salinity, from clean water to sea conditions; the surface contamination, with any soluble surfactant.

Acknowledgements

We thank Dan Ruth and Ricard Alert for fruitful discussion, Demetra Yancopoulos for participation in preliminary experiments, through the High Meadows Environmental Institute summer of learning program. We thank the three anonymous reviewers whose comments have helped improve the quality of the manuscript. This work was supported by the National Science Foundation (Physical Oceanography) under Grant No. 1849762 to L.D.; the Cooperative Institute for Earth System modeling between Princeton and GFDL NOAA; the Princeton Catalysis Initiative and the High Meadows Environmental Institute.

Declaration of Interests

The authors report no conflict of interest.

Appendix A. Surface bubble detection

The detection of isolated bubbles at the surface of water does not present technical difficulties. However, when bubbles assemble in rafts and touch each other, the only way to detect them unambiguously is to use their inner contour. Figure 27 presents the mode of operation. Figure 27a shows surface bubbles in a cluster, along with the detection of their inner edges. We then carefully select, from data acquired under the same conditions of lighting, a set of isolated bubbles of various sizes, as the one exhibited in figure 27b, over which both inner (d_m) and outer (d_s) diameters are measured. We finally use a linear fit to calibrate, in the dense regime, the actual size of the bubbles d_s , given the measured inner diameter d_m . Figure 27c shows an example of such a plot of d_s as a function of d_m , and the best linear fit associated.

REFERENCES

- AITKEN, J. 1880 On Dust, Fogs, and Clouds. *Trans. R. Soc. Edinburgh* **XX**, 337–368.
- ATASI, O., LEGENDRE, D., HAUT, B., ZENIT, R. & SCHEID, B. 2020 Lifetime of Surface Bubbles in Surfactant Solutions. *Langmuir* **36** (27), 7749–7764.
- BERNY, A., DEIKE, L., SÉON, T. & POPINET, S. 2020 Role of all jet drops in mass transfer from bursting bubbles. *Phys. Rev. Fluids* **5**, 033605.
- BERRY, J. D., NEESON, M. J., DAGASTINE, R. R., CHAN, D. Y. C. & TABOR, R. F. 2015 Measurement of surface and interfacial tension using pendant drop tensiometry. *J. Colloid Interface Sci.* **454**, 226–237.
- BLANCHARD, D. C. 1954 Bursting of Bubbles at an Air–Water Interface. *Nature* **173** (4413), 1048.
- BLANCHARD, D. C. & SYZDEK, L. D. 1988 Film Drop Production as a Function of Bubble Size. *J. Geophys. Res. Oceans* **93** (C4), 3649–3654.

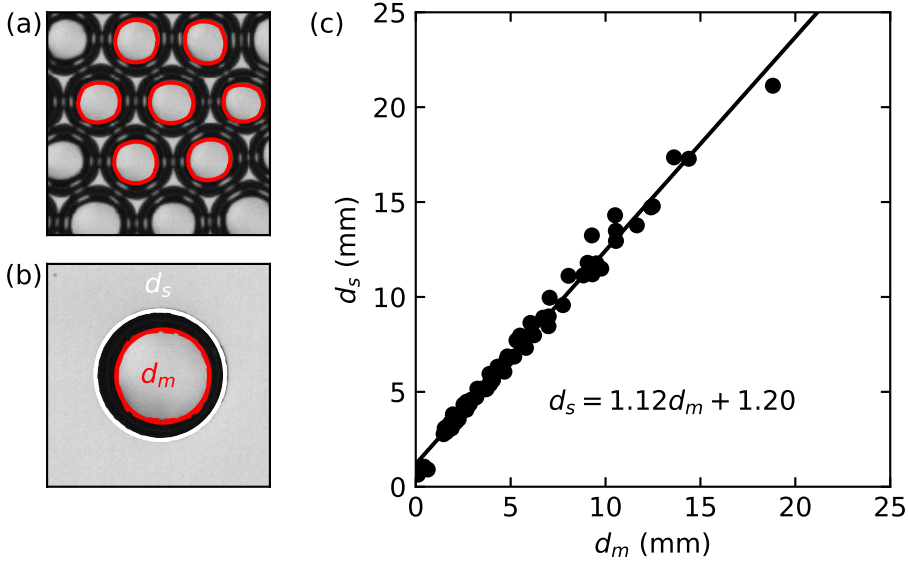


Figure 27: Bubbles detection and calibration in the raft regime. (a) Bubbles inner edges detection in a cluster. (b) Detection of the inner (red) and outer (white) edges of an isolated bubble. (c) Linear calibration from the inner diameter d_m to the bubble diameter d_s .

- BLANCO-RODRÍGUEZ, F. J. & GORDILLO, J. M. 2020 On the sea spray aerosol originated from bubble bursting jets. *J. Fluid Mech.* **886**, R2.
- BRAGG, W. L. & NYE, J. F. 1947 A dynamical model of a crystal structure. *Proc. R. Soc. Lond. A* **190** (1023), 474–481.
- BRASZ, C. FREDERIK, BARTLETT, CASEY T., WALLS, PETER L. L., FLYNN, ELENA G., YU, YINGXIAN ESTELLA & BIRD, JAMES C. 2018 Minimum size for the top jet drop from a bursting bubble. *Phys. Rev. Fluids* **3** (7), 074001.
- CANO-LOZANO, J. C., MARTÍNEZ-BAZÁN, C., MAGNAUDET, J. & TCHOUFAG, J. 2016 Paths and wakes of deformable nearly spheroidal rising bubbles close to the transition to path instability. *Phys. Rev. Fluids* **1** (5), 053604.
- CANTAT, I., COHEN-ADDAD, S., ELIAS, F., GRANER, F., HÖHLER, R., PITOIS, O., ROUYER, F. & SAINT-JALMES, A. 2013 *Foams: Structure and Dynamics*. Oxford University Press.
- CHAMPOUGNY, L., ROCHÉ, M., DRENCKHAN, W. & RIO, E. 2016 Life and death of not so “bare” bubbles. *Soft Matter* **12** (24), 5276–5284.
- CLIFT, R., GRACE, J. R. & WEBER, M. E. 1978 *Bubbles, Drops, and Particles*. Dover.
- COCHRAN, R. E., RYDER, O. S., GRASSIAN, V. H. & PRATHER, K. A. 2017 Sea Spray Aerosol: The Chemical Link between the Oceans, Atmosphere, and Climate. *Acc. Chem. Res.* **50** (3), 599–604.
- COLLINS, D. B., ZHAO, D. F., RUPPEL, M. J., LASKINA, O., GRANDQUIST, J. R., MODINI, R. L., STOKES, M. D., RUSSELL, L. M., BERTRAM, T. H., GRASSIAN, V. H., DEANE, G. B. & PRATHER, K. A. 2014 Direct aerosol chemical composition measurements to evaluate the physicochemical differences between controlled sea spray aerosol generation schemes. *Atmospheric Meas. Tech.* **7** (11), 3667–3683.
- COULIER, P.-J. 1875 Note sur une nouvelle propriété de l’air. *J. Pharm. Chim.* **22**, 165–173.
- CULICK, F. E. C. 1960 Comments on a Ruptured Soap Film. *J. Appl. Phys.* **31**, 1128–1129.
- DAVIDSON, J. F. & SCHÜLER, B. O. G. 1960 Bubble formation at an orifice in an inviscid liquid. *Trans. Inst. Chem. Eng.* **38**, 335–342.
- DE LEEUW, G., ANDREAS, E. L., ANGUELOVA, M. D., FAIRALL, C. W., LEWIS, E. R.,

- O'DOWD, C., SCHULZ, M. & SCHWARTZ, S. E. 2011 Production flux of sea spray aerosol. *Rev. Geophys.* **49** (2).
- DEIKE, L., GHABACHE, É., LIGER-BELAIR, G., DAS, A. K., ZALESKI, S., POPINET, S. & SÉON, T. 2018 Dynamics of jets produced by bursting bubbles. *Phys. Rev. Fluids* **3**, 013603.
- DEIKE, L., LENAIN, L. & MELVILLE, W. K. 2017 Air entrainment by breaking waves. *Geophys. Res. Lett.* **44**, 3779–3787.
- DEIKE, L. & MELVILLE, W. K. 2018 Gas Transfer by Breaking Waves. *Geophys. Res. Lett.* **45** (19), 10482–10492.
- DEIKE, L., MELVILLE, W. K. & POPINET, S. 2016 Air entrainment and bubble statistics in breaking waves. *J. Fluid Mech.* **801**, 91–129.
- DEMOTT, P. J., HILL, T. C. J., MCCLUSKEY, C. S., PRATHER, K. A., COLLINS, D. B., SULLIVAN, R. C., RUPPEL, M. J., MASON, R. H., IRISH, V. E., LEE, T., HWANG, C. Y., RHEE, T. S., SNIDER, J. R., McMEEKING, G. R., DHANIYALA, S., LEWIS, E. R., WENTZELL, J. J. B., ABBATT, J., LEE, C., SULTANA, C. M., AULT, A. P., AXSON, J. L., MARTINEZ, M. D., VENERO, I., SANTOS-FIGUEROA, G., STOKES, M. D., DEANE, G. B., MAYOL-BRACERO, O. L., GRASSIAN, V. H., BERTRAM, T. H., BERTRAM, A. K., MOFFETT, B. F. & FRANC, G. D. 2016 Sea spray aerosol as a unique source of ice nucleating particles. *Proc. Natl. Acad. Sci. U.S.A.* **113** (21), 5797–5803.
- DUCHEMIN, L., POPINET, S., JOSSEAND, C. & ZALESKI, S. 2002 Jet formation in bubbles bursting at a free surface. *Phys. Fluids* **14** (9), 3000–3008.
- DUINEVELD, P. C. 1995 The rise velocity and shape of bubbles in pure water at high Reynolds number. *J. Fluid Mech.* **292**, 325–332.
- ERININ, M. A., WANG, S. D., LIU, R., TOWLE, D., LIU, X. & DUNCAN, J. H. 2019 Spray Generation by a Plunging Breaker. *Geophys. Res. Lett.* **46** (14), 8244–8251.
- FAINERMAN, V. B., LYLYK, S. V., AKSENENKO, E. V., MAKIEVSKI, A. V., PETKOV, J. T., YORKE, J. & MILLER, R. 2009 Adsorption layer characteristics of Triton surfactants. *Colloids Surf. A* **334** (1), 1–15.
- FAINERMAN, V. B., LYLYK, S. V., AKSENENKO, E. V., PETKOV, J. T., YORKE, J. & MILLER, R. 2010 Surface tension isotherms, adsorption dynamics and dilational visco-elasticity of sodium dodecyl sulphate solutions. *Colloids Surf. A* **354** (1), 8–15.
- FAIRALL, C. W., KEPERT, J. D. & HOLLAND, G. J. 1994 The effect of sea spray on surface energy transports over the ocean. *Global Atmos. Ocean Syst.* **2**, 121–142.
- FRANKLIN, B. 1774 Of the stilling of waves by means of oil. *Phil. Trans.* **64**, 445–460.
- FROSSARD, A. A., LONG, M. S., KEENE, W. C., DUPLESSIS, P., KINSEY, J. D., MABEN, J. R., KIEBER, D. J., CHANG, R. Y.-W., BEAUPRÉ, S. R., COHEN, R. C., LU, X., BISGROVE, J. & ZHU, Y. 2019 Marine Aerosol Production via Detrainment of Bubble Plumes Generated in Natural Seawater With a Forced-Air Venturi. *J. Geophys. Res. Atmos.* **124** (20), 10931–10950.
- GAÑÁN-CALVO, A. M. 2017 Revision of Bubble Bursting: Universal Scaling Laws of Top Jet Drop Size and Speed. *Phys. Rev. Lett.* **119** (20), 204502.
- GARRETT, W. D. 1967 Stabilization of air bubbles at the air-sea interface by surface-active material. *Deep Sea Res.* **14** (6), 661–672.
- GHABACHE, É., ANTKOWIAK, A., JOSSEAND, C. & SÉON, T. 2014 On the physics of fizziness: How bubble bursting controls droplets ejection. *Phys. Fluids* **26**, 121701.
- GHABACHE, É., LIGER-BELAIR, G., ANTKOWIAK, A. & SÉON, T. 2016 Evaporation of droplets in a Champagne wine aerosol. *Sci. Rep.* **6**, 25148.
- GONNERMANN, H. M. & MANGA, M. 2007 The Fluid Mechanics Inside a Volcano. *Annu. Rev. Fluid Mech.* **39** (1), 321–356.
- JURIN, J. 1717 An Account of Some Experiments Shown before the Royal Society; With an Enquiry into the Cause of the Ascent and Suspension of Water in Capillary Tubes. *Phil. Trans.* **30** (351–363), 739–747.
- KULKARNI, A. A. & JOSHI, J. B. 2005 Bubble Formation and Bubble Rise Velocity in Gas-Liquid Systems: A Review. *Ind. Eng. Chem. Res.* **44** (16), 5873–5931.
- LAI, C.-Y., EGGERS, J. & DEIKE, L. 2018 Bubble Bursting: Universal Cavity and Jet Profiles. *Phys. Rev. Lett.* **121** (144501).

- LANGEVIN, D. & RIO, E. 2015 Foams and Emulsions: Coalescence. In *Encyclopedia of Surface and Colloid Science*, 3rd edn. (ed. P. Somasundaran), pp. 2837–2851. CRC Press.
- LENAIN, L. & MELVILLE, W. K. 2017 Evidence of Sea-State Dependence of Aerosol Concentration in the Marine Atmospheric Boundary Layer. *J. Phys. Oceanogr.* **47** (1), 69–84.
- LEVICH, V. G. 1962 *Physicochemical Hydrodynamics*, 2nd edn. Prentice-Hall.
- LEWIS, E. R. & SCHWARTZ, S. E. 2004 *Sea Salt Aerosol Production: Mechanisms, Methods, Measurements and Models-A Critical Review*. *Geophysical Monograph* 152. Washington, D.C.: American Geophysical Union.
- LHUISSIER, H. & VILLERMAUX, E. 2012 Bursting bubble aerosols. *J. Fluid Mech.* **696**, 5–44.
- LIU, X. & DUNCAN, J. H. 2006 An experimental study of surfactant effects on spilling breakers. *J. Fluid Mech.* **567**, 433–455.
- MAGNAUDET, J. & EAMES, I. 2000 The Motion of High-Reynolds-Number Bubbles in Inhomogeneous Flows. *Annu. Rev. Fluid Mech.* **32** (1), 659–708.
- MASON, B. J. 1971 *The Physics of Clouds*, 2nd edn. Clarendon Press.
- MODINI, R. L., RUSSELL, L. M., DEANE, G. B. & STOKES, M. D. 2013 Effect of soluble surfactant on bubble persistence and bubble-produced aerosol particles. *J. Geophys. Res. Atmos.* **118** (3), 1388–1400.
- MOUGIN, G. & MAGNAUDET, J. 2002 Path Instability of a Rising Bubble. *Phys. Rev. Lett.* **88** (1), 014502.
- MYSELS, K. J. 1986 Surface tension of solutions of pure sodium dodecyl sulfate. *Langmuir* **2** (4), 423–428.
- OOLMAN, T. O. & BLANCH, H. W. 1986 Bubble Coalescence in Stagnant Liquids. *Chem. Eng. Commun.* **43** (4-6), 237–261.
- PAULSEN, J. D., CARMIGNIANI, R., KANNAN, A., BURTON, J. C. & NAGEL, S. R. 2014 Coalescence of bubbles and drops in an outer fluid. *Nat. Commun.* **5**, ncomms4182.
- POULAIN, S. & BOUROUBA, L. 2019 Disease transmission via drops and bubbles. *Physics Today* **72** (5), 70–71.
- POULAIN, S., VILLERMAUX, E. & BOUROUBA, L. 2018 Ageing and burst of surface bubbles. *J. Fluid Mech.* **851**, 636–671.
- PRATHER, K. A., BERTRAM, TIMOTHY H., GRASSIAN, VICKI H., DEANE, GRANT B., STOKES, M. DALE, DEMOTT, PAUL J., ALUWIHARE, LIHINI I., PALENIK, BRIAN P., AZAM, FAROOQ, SEINFELD, JOHN H., MOFFET, RYAN C., MOLINA, MARIO J., CAPP, CHRISTOPHER D., GEIGER, FRANZ M., ROBERTS, GREGORY C., RUSSELL, LYNN M., AULT, ANDREW P., BALTRUSAITIS, JONAS, COLLINS, DOUGLAS B., CORRIGAN, CRAIG E., CUADRA-RODRIGUEZ, LUIS A., EBBEN, CARLENA J., FORESTIERI, SARA D., GUASCO, TIMOTHY L., HERSEY, SCOTT P., KIM, MICHELLE J., LAMBERT, WILLIAM F., MODINI, ROBIN L., MUI, WILTON, PEDLER, BYRON E., RUPPEL, MATTHEW J., RYDER, OLIVIA S., SCHOEPP, NATHAN G., SULLIVAN, RYAN C. & ZHAO, DEFENG 2013 Bringing the ocean into the laboratory to probe the chemical complexity of sea spray aerosol. *Proc. Natl. Acad. Sci. U.S.A.* **110** (19), 7550–7555.
- PRINCEN, H. M. 1963 Shape of a fluid drop at a liquid-liquid interface. *J. Colloid Sci.* **18** (2), 178–195.
- SAFFMAN, P. G. 1956 On the rise of small air bubbles in water. *J. Fluid Mech.* **1** (03), 249.
- SHAW, D. B. & DEIKE, L. 2021 Coalescence of Surface Bubbles. *J. Fluid Mech.* (in press).
- SPIEL, D. E. 1998 On the births of film drops from bubbles bursting on seawater surfaces. *J. Geophys. Res. Oceans* **103** (C11), 24907–24918.
- STEVENSON, P., ed. 2012 *Foam Engineering: Fundamentals and Applications*. Wiley & Sons.
- TAYLOR, G. I. 1959 The Dynamics of Thin Sheets of Fluid. III. Disintegration of Fluid Sheets. *Proc. Royal Soc. A* **253**, 313–321.
- TOBA, YOSHIAKI 1959 Drop Production by Bursting of Air Bubbles on the Sea Surface (II) Theoretical Study on the Shape of Floating Bubbles. *Journal of the Oceanographical Society of Japan* **15** (3), 121–130.
- VELLA, D. & MAHADEVAN, L. 2005 The “Cheerios effect”. *Am. J. Phys.* **73** (9), 817–825.
- VERGNIOLE, S. & BRANDEIS, G. 1996 Strombolian explosions: 1. A large bubble breaking at the surface of a lava column as a source of sound. *J. Geophys. Res. Solid Earth* **101** (B9), 20433–20447.

- VERON, F. 2015 Ocean Spray. *Annu. Rev. Fluid Mech.* **47**, 507–538.
- VERON, F., HOPKINS, C., HARRISON, E. L. & MUELLER, J. A. 2012 Sea spray spume droplet production in high wind speeds. *Geophys. Res. Lett.* **39** (16).
- VILLERMAUX, E. 2007 Fragmentation. *Annu. Rev. Fluid Mech.* **39**, 419–446.
- WANG, X., DEANE, G. B., MOORE, K. A., RYDER, O. S., STOKES, M. D., BEALL, C. M., COLLINS, D. B., SANTANDER, M. V., BURROWS, S. M., SULTANA, C. M. & PRATHER, K. A. 2017 The role of jet and film drops in controlling the mixing state of submicron sea spray aerosol particles. *Proc. Natl. Acad. Sci. U.S.A.* **114** (27), 6978–6983.
- WEAIRE, D. L. & HUTZLER, S. 1999 *The Physics of Foams*. Clarendon Press.
- WILSON, L. 1980 Relationships between pressure, volatile content and ejecta velocity in three types of volcanic explosion. *J. Volcanol. Geotherm. Res.* **8** (2), 297–313.
- WOODCOCK, A. H., KIENTZLER, C. F., ARONS, A. B. & BLANCHARD, D. C. 1953 Giant Condensation Nuclei from Bursting Bubbles. *Nature* **172** (4390), 1144–1145.
- WURL, O., WURL, E., MILLER, L., JOHNSON, K. & VAGLE, S. 2011 Formation and global distribution of sea-surface microlayers. *Biogeosciences* **8** (1), 121–135.
- YANG, Y. M. & MAA, J. R. 1984 Bubble coalescence in dilute surfactant solutions. *J. Colloid Interface Sci.* **98** (1), 120–125.
- ZENIT, R. & MAGNAUDET, J. 2008 Path instability of rising spheroidal air bubbles: A shape-controlled process. *Phys. Fluids* **20** (6), 061702.
- ZHENG, Q. A., KLEMAS, V. & HSU, Y.-H. L. 1983 Laboratory measurement of water surface bubble life time. *J. Geophys. Res. Oceans* **88** (C1), 701–706.